

## Clusters of Galaxies in the First Half of the Universe from the IRAC Shallow Survey

Peter R. M. Eisenhardt<sup>1</sup>, Mark Brodwin<sup>2</sup>, Anthony H. Gonzalez<sup>3</sup>, S. Adam Stanford<sup>4,5</sup>,  
Daniel Stern<sup>1</sup>, Pauline Barmby<sup>6</sup>, Michael J. I. Brown<sup>7</sup>, Kyle Dawson<sup>8</sup>, Arjun Dey<sup>2</sup>,  
Mamoru Doi<sup>9</sup>, Audrey Galametz<sup>1,10</sup>, B. T. Jannuzi<sup>2</sup>, C. S. Kochanek<sup>11</sup>, Joshua Meyers<sup>8,12</sup>,  
Tomoki Morokuma<sup>9,13</sup>, & Leonidas A. Moustakas<sup>1</sup>

### ABSTRACT

We have identified 335 galaxy cluster and group candidates, 106 of which are at  $z > 1$ , using a  $4.5\mu\text{m}$  selected sample of objects from a  $7.25\text{ deg}^2$  region in the *Spitzer* Infrared Array Camera (IRAC) Shallow Survey. Clusters were identified as 3-dimensional overdensities using a wavelet algorithm, based on photometric

---

<sup>1</sup>Jet Propulsion Laboratory, California Institute of Technology, MS 169-327, 4800 Oak Grove Drive, Pasadena, CA 91109, Peter.Eisenhardt@jpl.nasa.gov

<sup>2</sup>National Optical Astronomy Observatory, 950 North Cherry Avenue, Tucson, AZ 85719

<sup>3</sup>Department of Astronomy, University of Florida, Gainesville, FL 32611

<sup>4</sup>University of California, Davis, CA 95618

<sup>5</sup>Institute of Geophysics and Planetary Physics, Lawrence Livermore National Laboratory, Livermore, CA 94550

<sup>6</sup>Department of Physics and Astronomy, University of Western Ontario, 1151 Richmond St., London, ON N6A 3K7

<sup>7</sup>School of Physics, Monash University, Clayton, Victoria 3800, Australia

<sup>8</sup>E.O. Lawrence Berkeley National Laboratory, 1 Cyclotron Rd., Berkeley, CA 94720.

<sup>9</sup>Institute of Astronomy, Graduate School of Science, University of Tokyo 2-21-1 Osawa, Mitaka, Tokyo 181-0015, Japan

<sup>10</sup>Observatoire Astronomique de Strasbourg, 11 rue de l'Université, 67000 Strasbourg, France

<sup>11</sup>Department of Astronomy, Ohio State University, 140 West 18th Avenue, Columbus, OH 43210

<sup>12</sup>Department of Physics, University of California, Berkeley, CA 94720

<sup>13</sup>National Astronomical Observatory of Japan, 2-21-1 Osawa, Mitaka, Tokyo 181-8588, Japan

redshift probability distributions derived from IRAC and NOAO Deep Wide-Field Survey data. We estimate only  $\sim 10\%$  of the detections are spurious. To date 12 of the  $z > 1$  candidates have been confirmed spectroscopically, at redshifts from 1.06 to 1.41. Velocity dispersions of  $\sim 750 \text{ km s}^{-1}$  for two of these argue for total cluster masses well above  $10^{14} M_{\odot}$ , as does the mass estimated from the rest frame near infrared stellar luminosity. Although not selected to contain a red sequence, some evidence for red sequences is present in the spectroscopically confirmed clusters, and brighter galaxies are systematically redder than the mean galaxy color in clusters at all redshifts. The mean  $I - [3.6]$  color for cluster galaxies up to  $z \sim 1$  is well matched by a passively evolving model in which stars are formed in a 0.1 Gyr burst starting at redshift  $z_f = 3$ . At  $z > 1$ , a wider range of formation histories is needed, but higher formation redshifts (i.e.  $z_f > 3$ ) are favored for most clusters.

*Subject headings:* galaxies: clusters: general — infrared: surveys

## 1. Introduction

As the most massive gravitationally bound systems in the Universe, the rate of emergence of galaxy clusters since the Big Bang might be expected to be among the most straightforward predictions of cosmological models. Yet despite the advent of the era of precision cosmology ushered in by observations of SNe and the cosmic microwave background (CMB), significant uncertainty remains in the expected numbers of galaxy clusters at  $z > 1$ . The CMB temperature anisotropies on scales corresponding to clusters are not accurately known, leading to a range of values for  $\sigma_8$ , the rms matter fluctuation in a sphere of radius  $8h^{-1}$  Mpc at  $z = 0$ . Estimates of  $\sigma_8$  vary significantly, including e.g.  $0.67^{+0.18}_{-0.13}$  (Gladders et al. 2007),  $0.76 \pm 0.05$  (Spergel et al. 2007),  $0.80 \pm 0.1$  (Hettterscheidt et al. 2007),  $0.85 \pm 0.06$  (Hoekstra et al. 2006),  $0.90 \pm 0.1$  (Spergel et al. 2003),  $0.92 \pm 0.03$  (Hoekstra et al. 2002), and  $0.98 \pm 0.1$  (Bahcall & Bode 2003). The range  $\sigma_8 = 0.7$  to 1 corresponds to a variation of a factor of nearly 20 in the predicted numbers of  $z > 1$  clusters with  $M_{\text{tot}} > 10^{14} M_{\odot}$  (e.g. Sheth & Tormen 1999). Removing this uncertainty is a major goal of upcoming Sunyaev-Zeldovich cluster surveys such as the SZA (Sunyaev-Zeldovich Array; Loh et al. 2005), AMI (Arcminute Microkelvin Imager; Kneissl et al. 2001), ACT (Atacama Cosmology Telescope; Kosowsky 2003), and SPT (South Pole Telescope; Ruhl et al. 2004).

Since by definition<sup>1</sup> galaxy clusters contain an unusually high density of galaxies, they

---

<sup>1</sup>There is no generally agreed upon definition for galaxy clusters: see e.g. Abell (1958), Postman et al.

provide an efficient means of observing substantial numbers of galaxies at a common distance, offering the hope of constructing the analog of the Hertzsprung-Russell (i.e. color-magnitude) diagram for galaxy evolution. Indeed, studies of the relationship between color and magnitude indicate that clusters are the habitat of galaxies with the oldest and most massive stellar populations (e.g. Stanford, Eisenhardt, & Dickinson 1998; Blakeslee et al. 2003), objects reasonably free of the complications associated with starbursts and dust. These studies are consistent with an extremely simple formation history for cluster galaxies, in which their stars are formed in a short burst at high redshift, and they evolve quiescently thereafter (we use the term “red spike model” in referring to this scenario - see Figure 1). Studies of the near-IR luminosity functions of cluster galaxies reinforce this picture (e.g. de Propris et al. 1999; De Propris et al. 2007; Toft et al. 2004; Strazzullo et al. 2006). With their large look-back times, therefore, high redshift galaxy clusters also provide an observational pillar for our understanding of the formation and evolution of galaxies.

Obtaining substantial samples of galaxy clusters at  $z > 1$  has proved challenging, largely because such objects are difficult to detect using only optical data. Due to their greatly enhanced rate of star formation by  $z \sim 1$ , the UV emission from modest sized field galaxies overwhelms that from the intrinsically red spectra of quiescent, early type galaxies preferentially found in clusters. The Red Sequence Cluster Survey (Gladders & Yee 2000, 2005) uses the observed color-magnitude relationship in cluster galaxies to improve the contrast and has proven highly efficient to  $z \sim 1$ , but the optical colors of the red sequence become increasingly degenerate at higher redshifts, as they no longer span the rest 4000Å break. Wilson et al. (2006) describe a program to extend the red sequence technique to higher redshift using Spitzer data, but it is also important to *test* for the existence of red sequences in  $z > 1$  clusters rather than preselecting for them, if possible.

The contrast of high redshift clusters over the field improves at longer wavelengths (Figure 1), but the contrast against atmospheric emission declines, and until recently the relatively small formats of infrared detector arrays made surveying sufficient  $z \gtrsim 1$  volume a formidable undertaking. Stanford et al. (1997) reported the discovery of a cluster at  $z = 1.27$  in a 100 square arcminute survey to  $K_s(\text{Vega}) = 20$  ( $10\sigma$ ). But this survey required approximately 2 hours of exposure in both  $J$  and  $K_s$  per position, and 30 allocated nights of KPNO 4m time to complete. With estimates for the surface density of  $10^{14}M_\odot$  clusters at  $z > 1$  in the range 0.2 – 4 per square degree (Sheth & Tormen 1999), the discovery was in hindsight fortuitous.

---

(1996), and Rosati et al. (2002). We define our criteria for candidate galaxy clusters and groups in §5, and for spectroscopically confirmed candidates in §6.

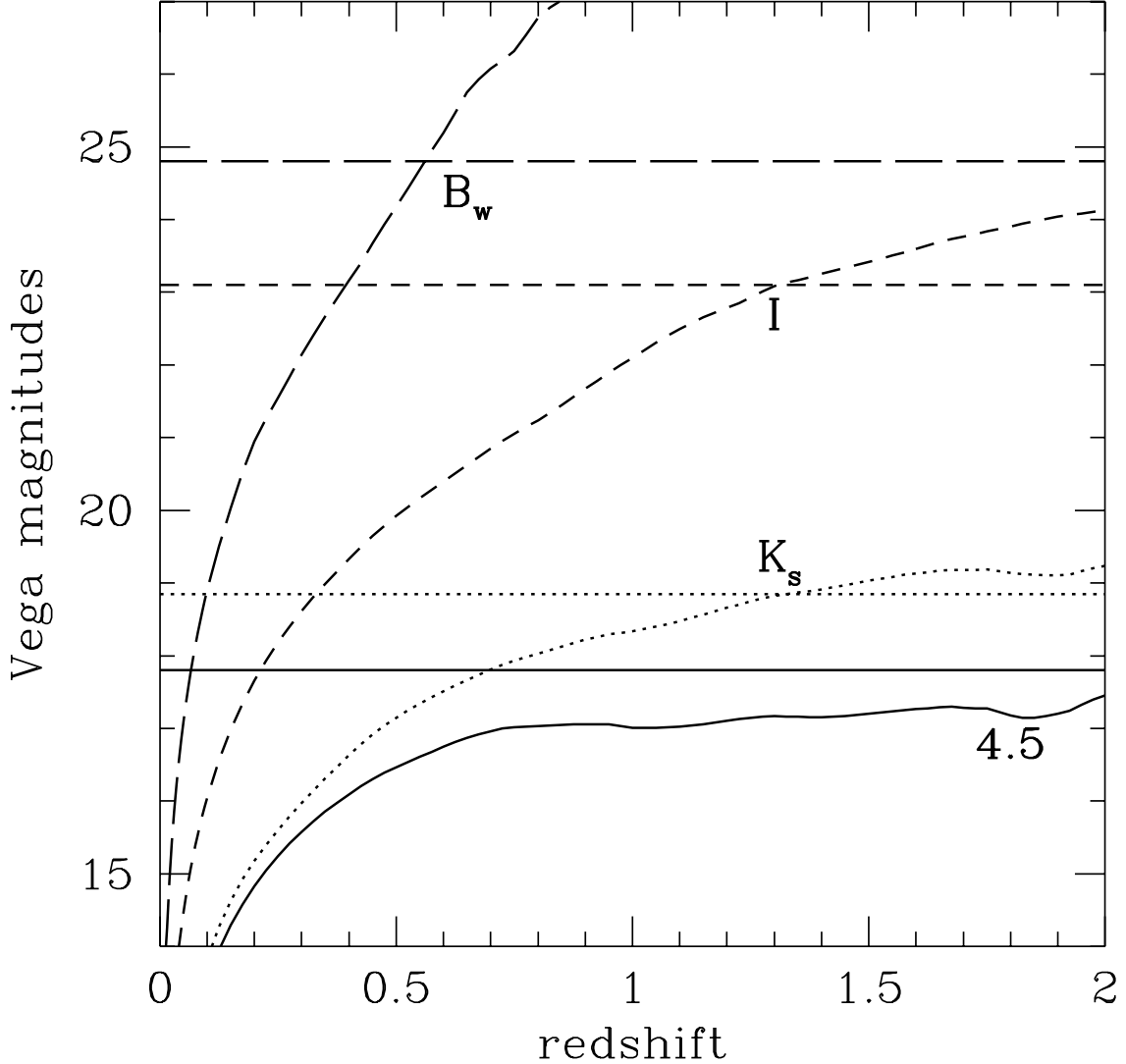


Fig. 1.—  $L^*$  for cluster galaxies vs.  $z$ , in the observed  $B_w$  (long dashed),  $I$  (short dashed),  $K_s$  (dotted), and IRAC  $4.5\mu\text{m}$  (solid) bands. The curves are based on a Bruzual & Charlot (2003) model where stars are formed in a 0.1 Gyr burst beginning at  $z_f = 3$  in a  $\Lambda = 0.7$ ,  $\Omega_m = 0.3$ ,  $h = 0.7$  cosmology, which fits the observed  $L^*$  in galaxy clusters to  $z \gtrsim 1$  (de Propris et al. 1999). This model is referred to as the “red spike” model in the text. Horizontal lines show the  $5\sigma$  limits of the IRAC Shallow Survey, FLAMEX survey, and NDWFS in  $5''$  diameter apertures. Note a  $5''$  aperture is larger than optimum for detection at  $B_w$  and  $I$ , and the 50% completeness limits in these bands are about 2 mag fainter.

Such considerations motivated a different approach, where extended sources in deep X-ray surveys lacking prominent optical counterparts were targeted for IR followup. This technique yielded confirmed clusters at  $z = 1.10$ ,  $1.23$ , and  $1.26$  (Stanford et al. 2002; Rosati et al. 1999, 2004). With the arrival of *XMM*, X-ray surveys offer renewed promise, leading recently to the identification of galaxy clusters at  $z = 1.39$  (Mullis et al. 2005) and  $1.45$  (Stanford et al. 2006). With exposure times  $> 20$  ksec and a 30 arcmin field of view, a discovery rate of approximately 30 hours per candidate  $z > 1$  cluster above  $10^{14}M_{\odot}$  is expected (assuming one such cluster per square degree, which corresponds to  $\sigma_8 = 0.83$ ).

Searches for clusters around radio galaxies have yielded protoclusters with redshifts as high as 4.1 (Pentericci et al. 2000; Venemans et al. 2002, 2005) and possibly even 5.2 (Overzier et al. 2006). The very large redshifts of these systems enable powerful inferences to be drawn regarding the formation of cluster galaxies, but they are less useful as probes of the cosmological growth of structure. Lyman Break Galaxy surveys with intensive followup spectroscopy on the Keck telescopes have also identified highly overdense structures at  $z = 2.30$  and  $3.09$  (Steidel et al. 1998, 2005), and Ouchi & SXDS (2007) discuss a  $z = 5.7$  structure identified via Ly- $\alpha$  emission in a narrow band imaging survey.

Recent advancements in IR detector array formats have renewed interest in ground-based IR surveys. In one example of the state of the art, Elston, Gonzalez et al. (2006) use the  $2048 \times 2048$  pixel FLAMINGOS camera to map  $4 \text{ deg}^2$  to a 50% completeness limit of  $K_s = 19.2$  (Vega). With 2 hour exposures on the KPNO 2.1m each covering  $1/10\text{th deg}^2$ , this leads to an expected discovery rate for high redshift clusters per useful hour of observing which is similar to *XMM*. The UKIDSS Ultra Deep Survey provides another recent example, finding 13 cluster candidates with  $0.6 < z < 1.4$  in a  $0.5 \text{ deg}^2$  survey (van Breukelen et al. 2006), one of which has 4 spectroscopic redshifts at  $z = 0.93$  (Yamada et al. 2005), and Zatloukal et al. (2007) find 12 candidates with  $1.23 < z < 1.55$  in a  $0.66 \text{ deg}^2$  *H*-band survey in the COSMOS field. McCarthy et al. (2007) present a system with a high density of galaxies with red optical to near-IR colors surrounding a galaxy at  $z = 1.51$ , identified in the  $120 \text{ arcmin}^2$  Gemini Deep Deep Survey. Candidates drawn from surveys of less than a square degree are unlikely to include many rich clusters, however.

With the launch of the *Spitzer Space Telescope* in 2003 (Werner et al. 2004), sensitive infrared arrays free from foreground thermal emission were put into operation (Fazio et al. 2004b). A major scientific driver for the *Spitzer* Infrared Array Camera (IRAC) Shallow Survey (Eisenhardt et al. 2004) was the detection of  $z > 1$  galaxy clusters. The IRAC Shallow Survey uses 90 second exposures per position and covers  $8.5 \text{ deg}^2$ , leading to an expected discovery rate of  $< 8$  hours per  $z > 1$  cluster. Here we present results from the IRAC Shallow Survey cluster search, finding 106 cluster and group candidates at  $z > 1$ , of

which we estimate only  $\sim 10\%$  are spurious.

A surface density of over 10 systems per square degree at  $z > 1$  is higher than expected for bound systems with masses above  $10^{14}M_{\odot}$  for the current range of plausible  $\sigma_8$  estimates. While we present evidence that at least two of the  $z > 1$  clusters have masses well above  $10^{14}M_{\odot}$ , it is likely that our sample includes systems with masses below  $10^{14}M_{\odot}$  (i.e. groups), and perhaps some unbound filaments viewed end-on. In the remainder of this paper, for brevity the terms “clusters” and “candidates” are used to refer to all such objects which meet our selection criteria, unless otherwise stated.

This paper describes how the cluster sample was identified, and some of the overall photometric properties of the sample. We also provide new spectroscopic evidence supporting nine of these clusters, from  $z = 1.057$  to  $1.373$ . Spectroscopic evidence in support of IRAC Shallow Survey selected clusters at  $z = 1.112$ ,  $1.243$ , and  $1.413$  was presented in Elston et al. (2006), Brodwin et al. (2006), and Stanford et al. (2005) respectively, and we provide additional previously unpublished spectroscopy on those clusters here, for completeness. Brodwin et al. (2007) discuss the clustering of the clusters, and Galametz et al. (in preparation) report on AGN incidence vs cluster-centric distance. Followup imaging with *HST* (GO 10496, Perlmutter; 10836, Stanford; and 11002, Eisenhardt) and *Spitzer* (GO 30950, Eisenhardt) is underway, and future papers will examine the scatter in the color-magnitude relation as a function of morphological type, the dependence of cluster galaxy size on redshift, starburst activity in clusters vs. redshift, and the dependence of mean galaxy properties on surface density.

A cosmology with  $H_0 = 70 \text{ km s}^{-1}$ ,  $\Omega_m = 0.3$ ,  $\Lambda = 0.7$  is assumed, and magnitudes are on the Vega system (defined in Reach et al. 2005, for IRAC). At  $z = 1 - 2$ , this means that one arcminute corresponds to a physical scale of  $480 - 502 \text{ kpc}$ , peaking at  $508 \text{ kpc}$  at  $z = 1.6$ . Unless otherwise specified, physical (rather than co-moving) scales are used throughout.

## 2. Data

### 2.1. IRAC Shallow Survey

The IRAC Shallow Survey (Eisenhardt et al. 2004) was designed to maximize the number of reliable sources detected per unit time and to cover sufficient area to detect significant numbers of  $z \gtrsim 1$  galaxy clusters. As explained in Eisenhardt et al. (2004), a 30 second exposure time per pointing is close to optimum for maximizing source detections, and reliability was obtained by requiring three independent exposures separated by hours at each position. The survey covers  $\approx 8.5 \text{ deg}^2$  and reaches an aperture-corrected  $5\sigma$  depth of  $\approx$

19.1 and 18.3 mag (Vega) at 3.6 and 4.5 $\mu$ m in 3'' diameter apertures. It is a remarkable fact that 90 seconds of combined exposure with IRAC on the 85 cm *Spitzer Space Telescope* provides sufficient sensitivity to detect evolving  $L^*$  galaxies to  $z = 2$  (Figure 1).

## 2.2. NOAO Deep Wide-Field Survey

The survey was carried out in the Boötes region of the NOAO Deep Wide-Field Survey (NDWFS; Jannuzi & Dey 1999) to allow photometric redshifts to be derived using the deep optical imaging available for this field. The NDWFS reaches  $5\sigma$  point-source depths in the  $B_W$ ,  $R$ , and  $I$  bands of  $\approx 27.1$ , 26.1, and 25.4 respectively. Typical exposure times per position with the Mosaic-1 camera on the KPNO Mayall 4-m telescope were 1 – 2 hours in  $B_W$ , 1 – 2 hours in  $R$ , and 2 – 4 hours in  $I$ , and the seeing ranged from 0.7 to 1.5''. The data acquisition, reduction, and catalog generation are discussed in detail by B. Jannuzi et al. (in preparation) and A. Dey et al. (in preparation). This paper uses the NDWFS third data release (DR3) images and SExtractor catalogs which can be obtained through the NOAO data archive<sup>2</sup>.

## 2.3. AGN and Galaxy Evolution Survey, FLAMINGOS Extragalactic Survey, and Other Surveys

The AGN and Galaxy Evolution Survey (AGES, C. Kochanek et al. in preparation) provides spectroscopic redshifts for  $\approx 17,000$  objects (using the version 2.0 catalog) in the IRAC Shallow Survey. AGES is highly complete for sources brighter than 15.7 mag at 4.5 $\mu$ m, and also for sources brighter than  $I = 18.5$ , with many redshifts for sources up to  $I = 20$ , enabling excellent assessment of the photometric redshifts to  $z \sim 0.5$  (Figure 1).

Deep near infrared imaging from the FLAMINGOS Extragalactic Survey (FLAMEX) is available for half the Boötes region (Elston et al. 2006), and was used for deriving a prior on the redshift likelihood functions (see §4).

Imaging of the Boötes NDWFS field has also been obtained in the radio (de Vries et al. 2002), at 24, 70, and 160 $\mu$ m with the MIPS instrument on *Spitzer* (Houck et al. 2005), in the  $z$ -band (Cool 2007), in the  $UV$  with *GALEX*, and in X-rays to a depth of 5 ksec with the ACIS instrument on the *Chandra X-ray Observatory* (Murray et al. 2005), but these data are not used in this paper.

---

<sup>2</sup><http://www.noao.edu/noao/noaodeep>

### 3. Sample

Object selection for the cluster search was carried out in the  $4.5\mu\text{m}$  band, because the negative K-correction as the rest-frame  $1.6\mu\text{m}$  peak shifts into this band leads to a flux which is nearly independent of redshift for  $0.7 < z < 2$  (Figure 1). Object detection and photometry was carried out using SExtractor (Bertin & Arnouts 1996) in double-image mode, allowing matched aperture photometry in the other IRAC bands. While smaller apertures maximize the depth of the survey, Monte Carlo simulations showed that  $5''$  diameter aperture magnitudes are necessary to provide sufficiently reliable color measurements and photometric redshifts (Brodwin et al. 2006). This flux limit ( $5\sigma$  at  $4.5\mu\text{m}$  in  $5''$ ) corresponds to  $13.3 \mu\text{Jy}$ , or a Vega-based magnitude of 17.8.

#### 3.1. Matching to the NDWFS Catalog

The NDWFS catalogs were also generated using SExtractor, but run in single-image mode in each band. Detections in the different optical bands and between the optical and IRAC catalogs were matched if the centroids were within  $1''$  of each other, using the closest optical source if more than one satisfied this criterion. For very extended objects (generally at  $z \leq 0.2$ ), detections in the different bands were matched if the centroids were within an ellipse defined using the second order moments of the light distribution of the object (Brown et al. 2005).

#### 3.2. $B_W\text{RI}[3.6]$ Flux Limits and Photometric Errors

The NDWFS data were taken over several years in variable conditions, and therefore the photometric depths vary somewhat from pointing to pointing. Average 50% completeness limits for the  $B_W$ ,  $R$ , and  $I$ -bands were 26.7, 25.6, and 25.0 respectively. Average  $5\sigma$  flux (magnitude) limits in a  $5''$  aperture (which is significantly larger than the optimum detection aperture for these data) were measured via Monte Carlo simulations to be  $0.45 \mu\text{Jy}$  (24.8 mag) in  $B_W$ ,  $1.03 \mu\text{Jy}$  (23.7 mag) in  $R$ , and  $1.45 \mu\text{Jy}$  (23.1 mag) in the  $I$ -band (Brodwin et al. 2006). In the space-based IRAC Shallow survey the depth is more uniform, and in the  $3.6\mu\text{m}$  band it is  $10.0 \mu\text{Jy}$  (18.6 mag), also derived from a Monte Carlo simulation.

Although the majority of objects in the  $4.5\mu\text{m}$ -selected catalog are well detected at shorter wavelengths, this is not generally the case for  $z > 1$  red ellipticals. Objects at these redshifts are often quite faint in the optical as the  $4000\text{\AA}$  break is longward of the  $I$ -band (see Figure 1). Where sources were observed but not detected, the flux was taken to be zero

and a Monte Carlo  $1\sigma$  error was adopted. This approach is optimal for photometric redshift fitting, where the non-detection provides important constraints on the galaxy spectral energy distribution (SED).

### 3.3. Sample for Photometric Redshift Estimation and Cluster Search

The photometry used for photometric redshift estimation (§4) consists of  $B_W RI[3.6][4.5]$  data with the Monte Carlo photometric errors and limits noted above. The  $5.8\mu\text{m}$  and  $8.0\mu\text{m}$  bands were not used because they do not have the sensitivity to detect  $z > 1$  cluster  $L^*$  galaxies in the IRAC Shallow Survey. While the IRAC Shallow Survey covers  $8.5 \text{ deg}^2$  in each band, the overlap area observed in both the  $3.6$  and  $4.5\mu\text{m}$  IRAC bands is  $8.0 \text{ deg}^2$ . All of this falls within the optical NDWFS Boötes region. However, due to haloes around bright objects, shorter observation times for regions at the edges of individual mosaic camera pointings, and residual CCD defects,  $0.75 \text{ deg}^2$  may have lower quality optical photometry and hence photometric redshifts. Hence these regions are also excluded from the sample.

Finally, 14,044 stars were removed from the catalog using the SExtractor stellarity index in the best seeing optical data for each location. Comparison to the star count model of Arendt et al. (1998), as tabulated in Fazio et al. (2004a), suggests that  $\sim 80\%$  of stars were identified via this approach, leaving  $\sim 2\%$  of the  $4.5\mu\text{m}$  sample as unrecognized stars.

In summary, photometric redshifts were estimated for a total of 175,431 objects brighter than  $13.3 \mu\text{Jy}$  ( $5\sigma$ ) at  $4.5\mu\text{m}$  in  $5''$  in a  $7.25 \text{ deg}^2$  region.

## 4. Photometric Redshifts

A full description of the photometric redshift methodology is given in Brodwin et al. (2006). A summary of those aspects most relevant to cluster detection is provided here. Photometric redshifts were computed using an empirical template-fitting algorithm which linearly interpolates between the four Coleman, Wu, & Weedman (1980) SEDs (E, Sbc, Scd, and Im), augmented by the Kinney et al. (1996) SB3 and SB2 starburst templates. These SEDs were extended to the far-UV and near-IR using Bruzual & Charlot (2003) models. These stellar photospheric models do not include emission from dust, in particular the PAH features which dominate the  $3 < \lambda < 12\mu\text{m}$  portion of the spectrum in starforming galaxies, but at  $z > 1$  the photometry used does not sample these rest wavelengths.

In addition to the large AGES (C. Kochanek et al. in preparation) survey, there are  $\sim 500$  spectroscopic redshifts extending to  $z \sim 1.5$  gleaned from several ongoing surveys in

the Boötes field. These were used as training sets to adjust the templates and photometric zero points to improve overall redshift accuracy and reliability (see Brodwin et al. 2006, for details). Comparison with these spectroscopic samples shows that an rms dispersion of  $\sigma_z \sim 0.06(1 + z)$  is achieved for 95% of galaxies to at least  $z = 1.5$ . Subsequent follow-up spectroscopy of high redshift candidate clusters (§6.2; see also Stanford et al. 2005; Brodwin et al. 2006; Elston et al. 2006) verify this accuracy.

A key output of the Brodwin et al. (2006) technique is the redshift probability function for each object,  $P(z)$ , derived directly from the redshift-axis projection of the full redshift–SED likelihood surface. To transform these simple redshift likelihood functions into true probability distribution functions, a prior consisting of the observed redshift distribution was applied. This was measured in the FLAMEX region using high-quality  $B_wRIJK_s[3.6][4.5]$  photometric redshifts. Comparison to the spectroscopic sample illustrates that the resulting distribution functions are statistically valid in the sense that integrated areas accurately represent redshift probabilities at the 1, 2, and  $3\sigma$  levels. These  $P(z)$  functions are the input to the wavelet detection algorithm discussed in §5 and are also used in §7.

Note that the  $P(z)$  distributions shows relatively little dependence on galaxy type (Brodwin et al. 2006). The reason is that while all galaxies are selected to have at least 5 sigma detections in [4.5], red galaxies are often only marginally detected or even undetected in our optical images, since they have very little blue light. This is particularly true at  $z > 1$  where the  $k$ -correction for early types is large in the optical. Blue galaxies have good  $B_wRI[3.6][4.5]$  photometry, because they have more blue light. Thus even though blue, late-type galaxy SED’s have smaller breaks, they have more extensive (useful) photometry. These compensating effects lead to effectively type-independent photometric redshifts for  $z > 1$  galaxies.

## 5. Cluster Detection

We employed a wavelet analysis to identify galaxy clusters within the Boötes region. Wavelet decomposition is a commonly used technique for cluster identification in X-ray images (for example, see Vikhlinin et al. 1998; Valtchanov et al. 2004; Andreon et al. 2005; Kenter et al. 2005), where it provides an effective means of identifying extended sources in the presence of contaminating point sources. In principle, a similar analysis can be used with optical and infrared data sets, using galaxies rather than X-ray photons to identify extended sources. As is well known, galaxy number counts are more susceptible to projection effects than is bremsstrahlung emission from the ICM. This issue is one that must be dealt with for all optical and infrared cluster searches, and consequently most such searches

for distant clusters make explicit assumptions about the properties of the distant cluster population, such as an assumed density profile (e.g., Postman et al. 1996; Olsen et al. 1999; Scodreggio et al. 1999) or the presence of a red sequence (Gladders & Yee 2000, 2005). The SDSS C4 technique (Miller et al. 2005) does not require a *red* sequence, but it does demand that the colors of cluster galaxies are similar to one another.

A significant advantage of the Boötes data set is that the photometric redshifts permit such assumptions to be minimized. The full photometric redshift probability distributions  $P(z)$  were used to construct weighted galaxy density maps within overlapping redshift slices of width  $\Delta z = 0.2$ , stepping through redshift space in increments of  $\delta z = 0.1$ . For each galaxy the weight in the map corresponds to the probability that the galaxy lies within the given redshift slice. Weighting in this fashion de-emphasizes sources for which the redshift is poorly constrained. It is worth emphasizing that *all* galaxies were included in construction of the density map, and consequently cluster detection should be relatively independent of SED type and hence independent of morphology. Finally, cluster detection will be insensitive to the resolution of the density maps provided that the pixel size is small compared to the angular extent of cluster cores at all redshifts. A resolution of  $12''$  ( $\sim 100$  kpc) per pixel was used, which satisfies this criterion while being sufficiently large to keep computational overhead manageable.

Galaxy cluster candidates were detected within each redshift slice by convolving the density map with the wavelet kernel. We use a Gaussian difference kernel of the form

$$k(r) = \frac{e^{-r^2/(2\sigma_1^2)}}{\sigma_1^2} - \frac{e^{-r^2/(2\sigma_2^2)}}{\sigma_2^2}, \quad (1)$$

where  $\sigma_1 = 400$  kpc and  $\sigma_2 = 1600$  kpc, and which crosses zero near  $r = 1$  Mpc. The scale of the kernel is fixed in physical rather than angular units, preserving our ability to uniformly identify comparable systems at different redshifts. The precise physical values of  $\sigma$  are subject to refinement, but the selected values effectively isolate overdensities on the scale of clusters or groups.

Galaxy cluster candidates were detected in each redshift slice of these wavelet smoothed galaxy density maps using a simple peak-finding algorithm. To establish a consistent significance level for the candidates, 1000 bootstrap simulations were carried out within each redshift slice. The existing  $P(z)$  distributions, right ascensions, and declinations were repeatedly shuffled, convolved with the wavelet kernel, and candidates detected to find the threshold corresponding to one false positive per redshift slice within the Boötes field. A list of detections above this significance threshold was generated for each redshift slice. Because the right ascensions and declinations were shuffled independently, the true correlated background was not preserved. Consequently, the contamination rate may be somewhat higher

than the one false positive per redshift slice expected if we had preserved the correlated background. For the current analysis we accept the somewhat higher contamination rate in exchange for improved completeness, particularly for the highest redshift clusters. The majority of clusters are detected in multiple redshift slices (a natural consequence of sampling in slices separated by step sizes finer than the galaxy redshift uncertainties). Multiple detections with small separations in positions and redshift slices were considered to be a single cluster, which was assigned an estimated redshift and position corresponding to the slice with the highest statistical significance. A total of 335 candidates were found in redshift slices with centers from 0.1 to 1.9, including 98 in slices with  $z > 1$ .

While the detection technique is on three dimensional overdensities, it is not immune to projection effects. The expected number of clusters in each cylindrical bin of length  $\Delta z = 0.2$  and radius 1 Mpc (the radius of the wavelet detection kernel) was computed to quantify the extent of projection. This calculation included both the random expectation due to the observed number density and the excess clusters expected due to the observed clustering of this sample (Brodwin et al. 2007). The projection rate is most significant for lower redshifts because of the large angular size corresponding to 1 Mpc, affecting  $\sim 10\%$  of systems at  $z = 0.5$  to  $\sim 20\%$  at  $z = 0.1$ . The projection rate decreases to below  $\sim 4\%$  at  $z = 1$  and is negligible at  $z > 1.5$ . Overall we estimate that  $\sim 10\%$  of the candidates may be spurious, including the contamination noted in the previous paragraph.

## 6. Cluster Redshifts and Members

The peak of the summed  $P(z)$  distribution at the cluster detection location was taken as the initial estimate of each cluster’s redshift. To improve this estimate, individual objects within a 1 Mpc radius of the cluster which included the cluster redshift within the  $1\sigma$  range of their  $P(z)$  functions were considered candidate cluster members. A refined estimate ( $z_{\text{est}}$ ) of the mean cluster redshift was obtained from the peak of the summed  $P(z)$  distribution for these members. From this analysis, 104 candidates have  $z_{\text{est}} > 1$ .

In Table 1 and Figures 2 - 13 we present 12 of the cluster candidates that were detected via the above criteria, and subsequently spectroscopically confirmed at the Keck Observatory to lie at  $z > 1$  (see §6.2). Two of these, ISCS J1434.1+3328 and ISCS J1429.2+3357, have  $z_{\text{est}} = 0.98$  but the spectroscopic mean redshifts are  $z = 1.057$  and  $1.058$  respectively. Hence we report a total of 106 clusters at  $z > 1$ , of which roughly 10% may be expected to arise by chance or from projection effects, for the reasons noted in §5. Column 1 of Table 1 provides the catalog number of each cluster. The catalog numbers increase with decreasing detection

significance ( $\S 5$ )<sup>3</sup>. Column 2 is the IAU designation for each cluster, based on the (J2000) coordinates of the detection given in columns 3 and 4. Column 5 provides the  $z_{\text{est}}$  value described above, and column 6 gives the mean redshift of the spectroscopically confirmed members. Column 7 provides the number of photometric redshift members of the cluster, defined as galaxies within 1 Mpc of the cluster center and with integrated  $P(z) \geq 0.3$  in the range  $z_{\text{est}} \pm 0.06(1 + z_{\text{est}})$ . These galaxies are used to calculate mean cluster colors in  $\S 7.2$ . Column 8 reduces the number in column 7 by the number of galaxies which satisfy these criteria for each cluster redshift over the entire field, scaled to the 1 Mpc radius area for each cluster redshift. Column 9 gives the number of spectroscopically confirmed member galaxies in each cluster (see below). Column 10 gives the mean  $I - [3.6]$  color for the photometric redshift member galaxies, and column 11 provides the sum of their luminosities in  $[4.5]$  relative to an  $L^*$  value which evolves according to the “red spike” model shown in Figure 1, corrected for the average over the field. Column 12 gives the luminosity in  $[4.5]$  of the brightest photometric redshift member galaxy relative to  $L^*$ .

We define a  $z > 1$  cluster as spectroscopically confirmed if it contains at least 5 galaxies in the range  $z_{\text{est}} \pm 0.06(1 + z_{\text{est}})$  and within a radius of 2 Mpc, whose spectroscopic redshifts match to within  $\pm 2000(1 + \langle z_{\text{sp}} \rangle)$  km/s. The spectroscopic redshifts must also be of class A or B. Class A spectra have unambiguous redshift determinations, typically relying upon multiple well detected emission or absorption features. Class B spectral features are reliable but are less well detected. The radius threshold for spectroscopic membership is larger than the 1 Mpc used for photometric redshift members for practical reasons: most of the  $z > 1$  redshifts reported here were obtained with slitmasks extending out to approximately 2 Mpc from the cluster center. Typically  $< 10$  photometric redshift members within 1 Mpc could be accommodated in the mask design, and often no redshift could be determined from the resulting spectra.

The least significant cluster in Table 1 is ISCS J1434.5+3427, which is the 327th most significant detection out of the sample of 335, and the 100th most significant detection at  $z > 1$ . Despite its relatively low detection significance, ISCS J1434.5+3427 has a striking filamentary morphology (Figure 9), and has eleven spectroscopically confirmed members (see also Brodwin et al. 2006).

---

<sup>3</sup>These numbers extend beyond 335 for continuity with an earlier, preliminary version of the catalog used to plan spectroscopic and other followup observations.

Table 1.  $z > 1$  ISCS Clusters with Spectroscopic Confirmation<sup>a</sup>

Rank	ID	RA	Dec	$z_{\text{est}}$	$\langle z_{\text{sp}} \rangle$	$N_{\text{p}}$	$N_{\text{p}}(\text{bc})$	$N_{\text{sp}}$	$\langle I - [3.6] \rangle$	$L_{\text{tot}}/L^*$	$L_{\text{bcg}}/L^*$
152	ISCS_J1434.1+3328	14:34:10.37	+33:28:18.3	0.98	1.057	32	13	6	4.83	15	2.5
51	ISCS_J1429.2+3357	14:29:15.16	+33:57:08.5	0.98	1.058	45	26	7	4.80	34	4.2
19	ISCS_J1433.1+3334	14:33:06.81	+33:34:14.2	1.02	1.070	57	38	20	4.93	45	4.3
123	ISCS_J1433.2+3324	14:33:16.01	+33:24:37.4	1.01	1.096	31	11	6	4.94	15	4.6
17	ISCS_J1432.4+3332	14:32:29.18	+33:32:36.0	1.08	1.112	49	31	23	5.16	47	5.3
34	ISCS_J1426.1+3403	14:26:09.51	+34:03:41.1	1.08	1.135	31	13	7	5.18	26	4.0
14	ISCS_J1426.5+3339	14:26:30.42	+33:39:33.2	1.11	1.161	52	35	5	5.15	47	2.8
342	ISCS_J1434.5+3427	14:34:30.44	+34:27:12.3	1.20	1.243	27	12	11	5.51	27	6.0
30	ISCS_J1429.3+3437	14:29:18.51	+34:37:25.8	1.14	1.258	23	7	9	5.30	11	6.5
29	ISCS_J1432.6+3436	14:32:38.38	+34:36:49.0	1.24	1.347	30	17	8	5.65	31	4.3
25	ISCS_J1434.7+3519	14:34:46.33	+35:19:33.5	1.37	1.373	19	9	5	5.77	17	3.9
22	ISCS_J1438.1+3414	14:38:08.71	+34:14:19.2	1.33	1.413	25	15	10	5.75	24	3.5

<sup>a</sup>Columns are explained in §6

## 6.1. AGES Spectroscopy

The extensive AGES spectroscopic database (C. Kochanek et al. in preparation) can be used to spectroscopically confirm clusters at  $z < 0.5$ , a redshift at which  $L^*$  corresponds to  $I = 20$  (Figure 1), the magnitude limit for AGES spectroscopy. Note that while AGES is 94% complete to  $I = 18.5$ , sparse sampling is used for fainter galaxies, and currently spectra are available for  $\sim 40\%$  of galaxies with  $18.5 < I < 20$ . Because of the high surface density of AGES redshifts and the larger angular scale at  $z < 0.5$ , and the fact that the [4.5] flux limit samples substantially less luminous galaxies at these redshifts, two additions to the criteria for spectroscopic confirmation used at  $z > 1$  were imposed. To contribute to spectroscopic confirmation for cluster candidates with  $z_{\text{est}} < 0.5$ , galaxies were required to be more luminous than  $L^* + 1$  in [4.5] for a red spike evolving model. Also, the average surface density of AGES galaxies over the Boötes field which would satisfy our high redshift confirmation criteria was calculated as a function of redshift, and 5 galaxies above this field level were required for a cluster to be confirmed.

Of the 335 cluster candidates, 80 have  $z_{\text{est}} < 0.5$ . However seven lie near the edges of the Boötes field and hence were not well observed in AGES. Of the remaining 73, 61 candidates are confirmed by AGES spectroscopy using the criteria just described. This criterion is perhaps overly stringent: it rejects two clusters at  $z = 0.2$  with 17 or more matching AGES redshifts, but with only 4 (rather than 5) for galaxies brighter than  $L^* + 1$  after field correction. All of the other 10 candidates observed by AGES which do not meet the confirmation criteria have  $z_{\text{est}} \geq 0.37$ , and half have  $z_{\text{est}} \geq 0.45$ .

Given the sparse sampling of AGES at  $I > 18.5$ , which corresponds to  $L^*$  at  $z > 0.3$  (Figure 1), we believe this confirmation rate validates our estimate that only  $\sim 10\%$  of our cluster candidates arise by chance or due to projection effects. Further details on  $z < 1$  clusters will be provided in A. Gonzalez et al. (in preparation).

## 6.2. Keck Spectroscopy

Most of the high redshift spectroscopic confirmation of ISCS clusters has been obtained at Keck Observatory. Three clusters observed with Keck have been reported previously: ISCS J1432.4+3332 ( $z = 1.112$ ), ISCS J1434.5+3427 ( $z = 1.243$ ), and ISCS J1438.1+3414 ( $z = 1.413$ ) are presented in Elston et al. (2006), Brodwin et al. (2006), and Stanford et al. (2005), respectively. Here we provide spectroscopic confirmation for an additional nine clusters at  $z > 1$ , as well as some new spectroscopic information for the initial three clusters. Table 2 details new observations of ISCS clusters. Table 3 provides properties of previously

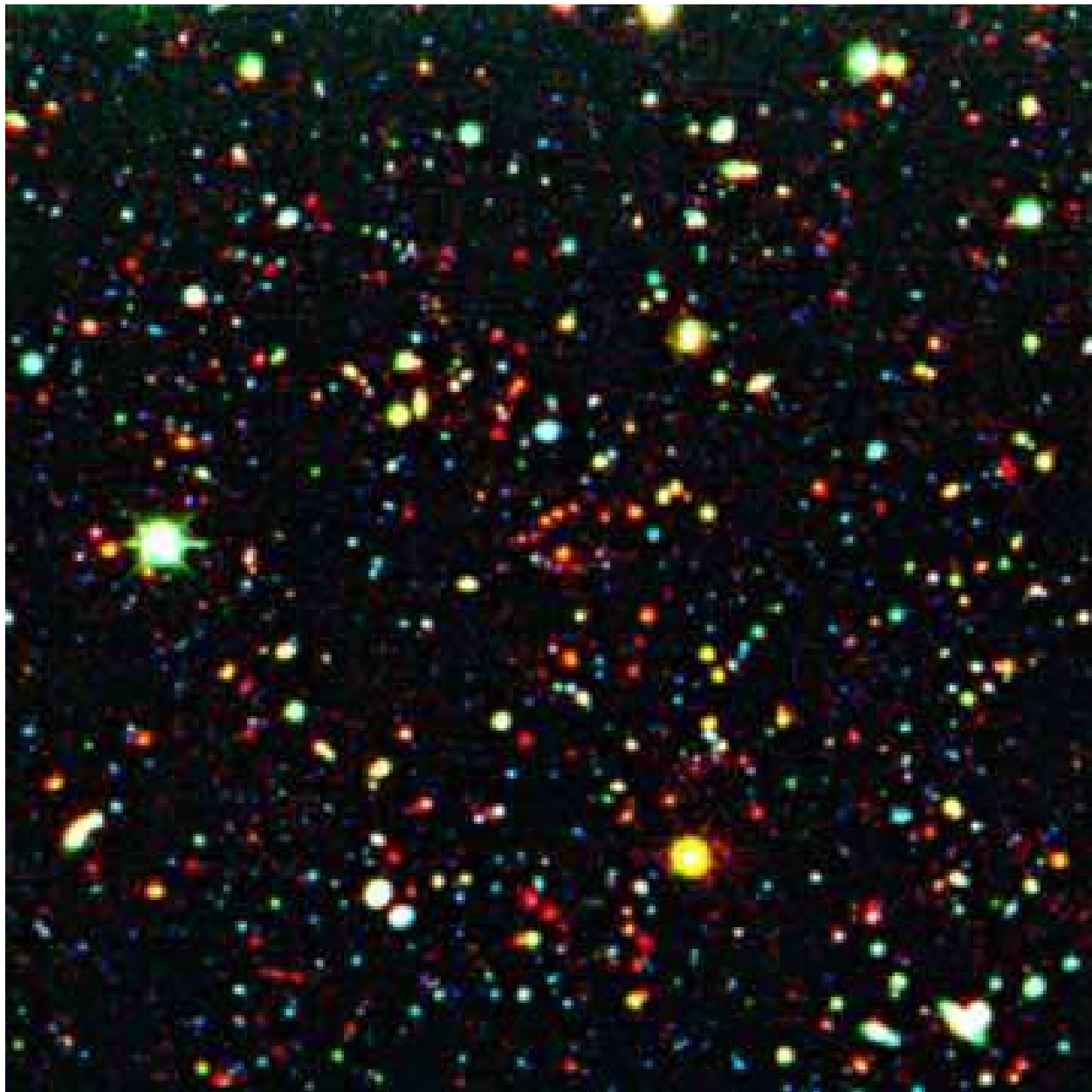


Fig. 2.— Composite NDWFS and *Spitzer* IRAC  $B_W$ ,  $I$ ,  $[4.5]$  color image of cluster ISCS J1434.1+3328 at  $\langle z_{\text{sp}} \rangle = 1.057$ . North is up and east is left, and the field size is  $5'$  square ( $\sim 2.4 - 2.5$  Mpc for  $z = 1 - 1.5$ ). The published version of these figures will label photometric redshift members, and spectroscopic members and non-members.

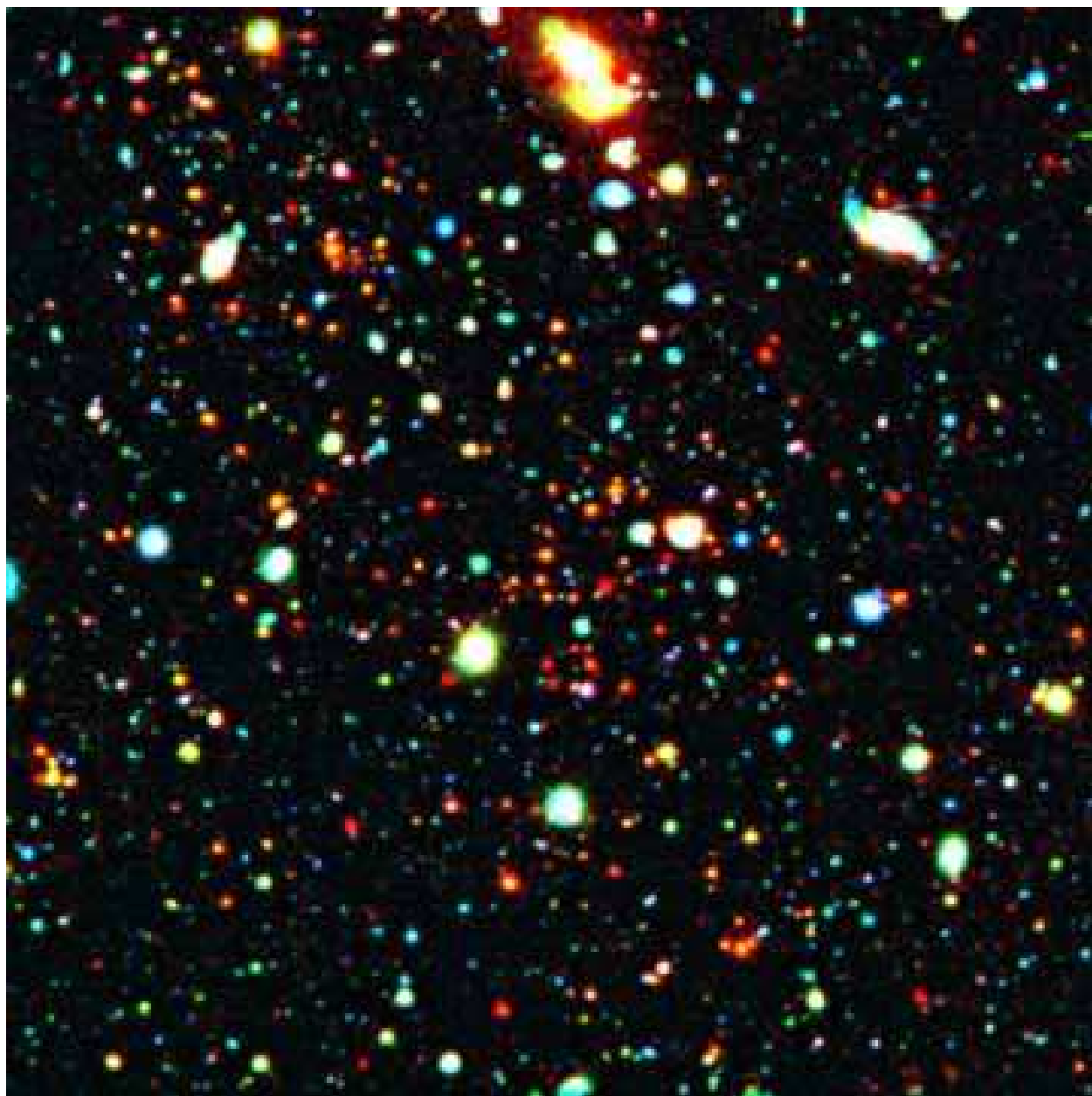


Fig. 3.— As for Figure 2, but for cluster ISCS J1429.2+3357 at  $\langle z_{\text{sp}} \rangle = 1.058$ .

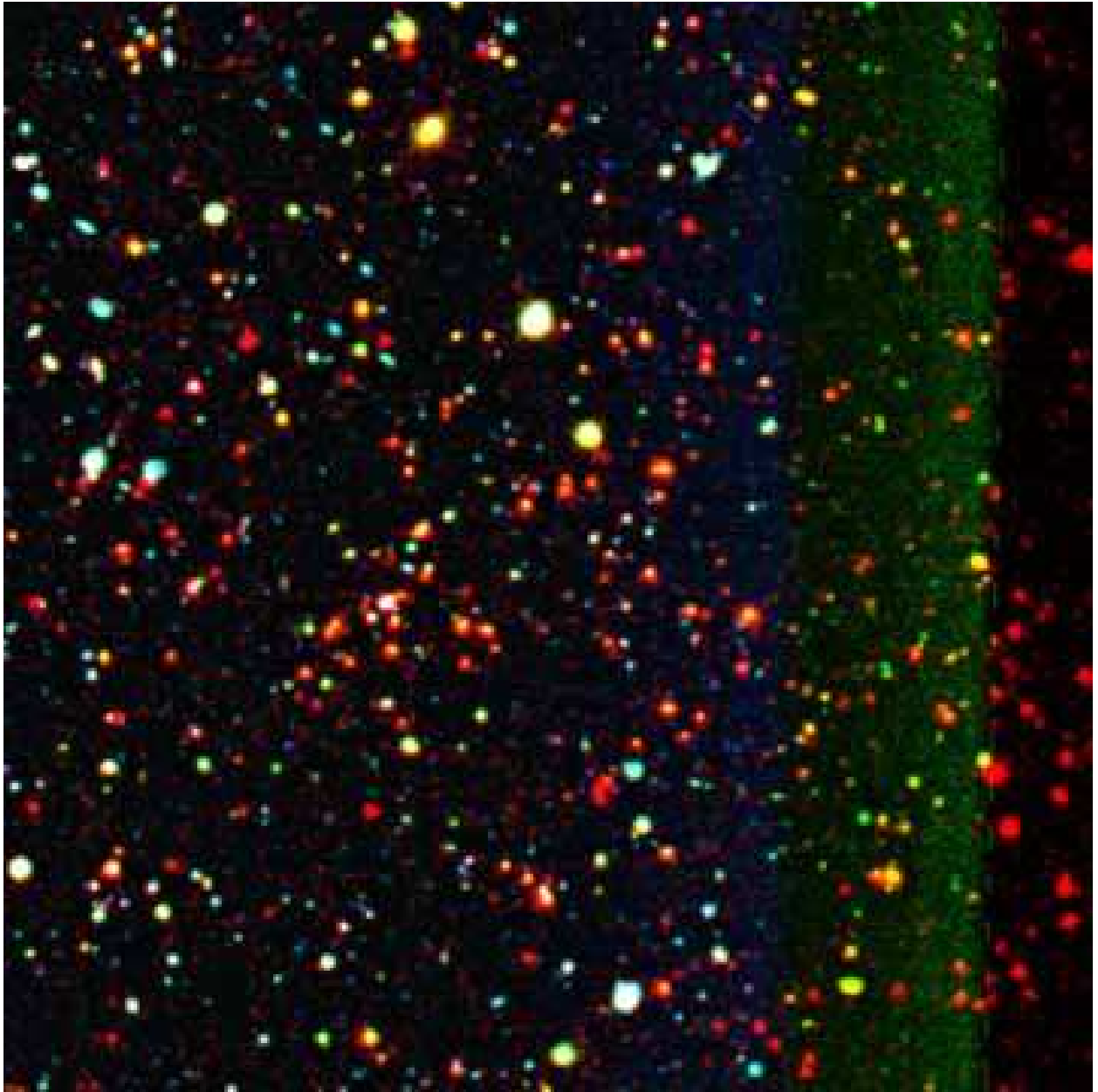


Fig. 4.— As for Figure 2, but for cluster ISCS J1433.1+3334 at  $\langle z_{\text{sp}} \rangle = 1.070$ .

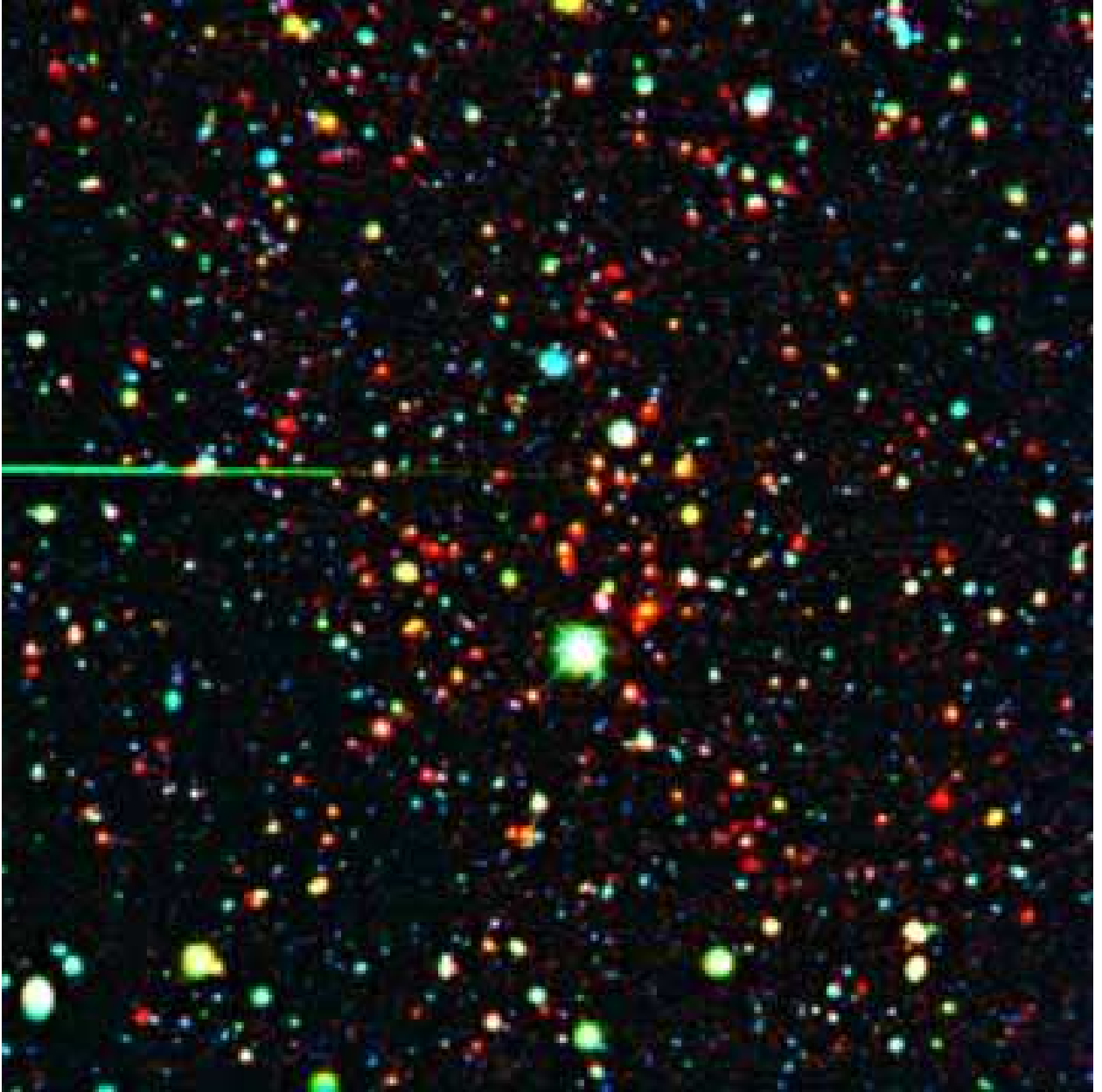


Fig. 5.— As for Figure 2, but for cluster ISCS J1433.2+3324 at  $\langle z_{\text{sp}} \rangle = 1.096$ .

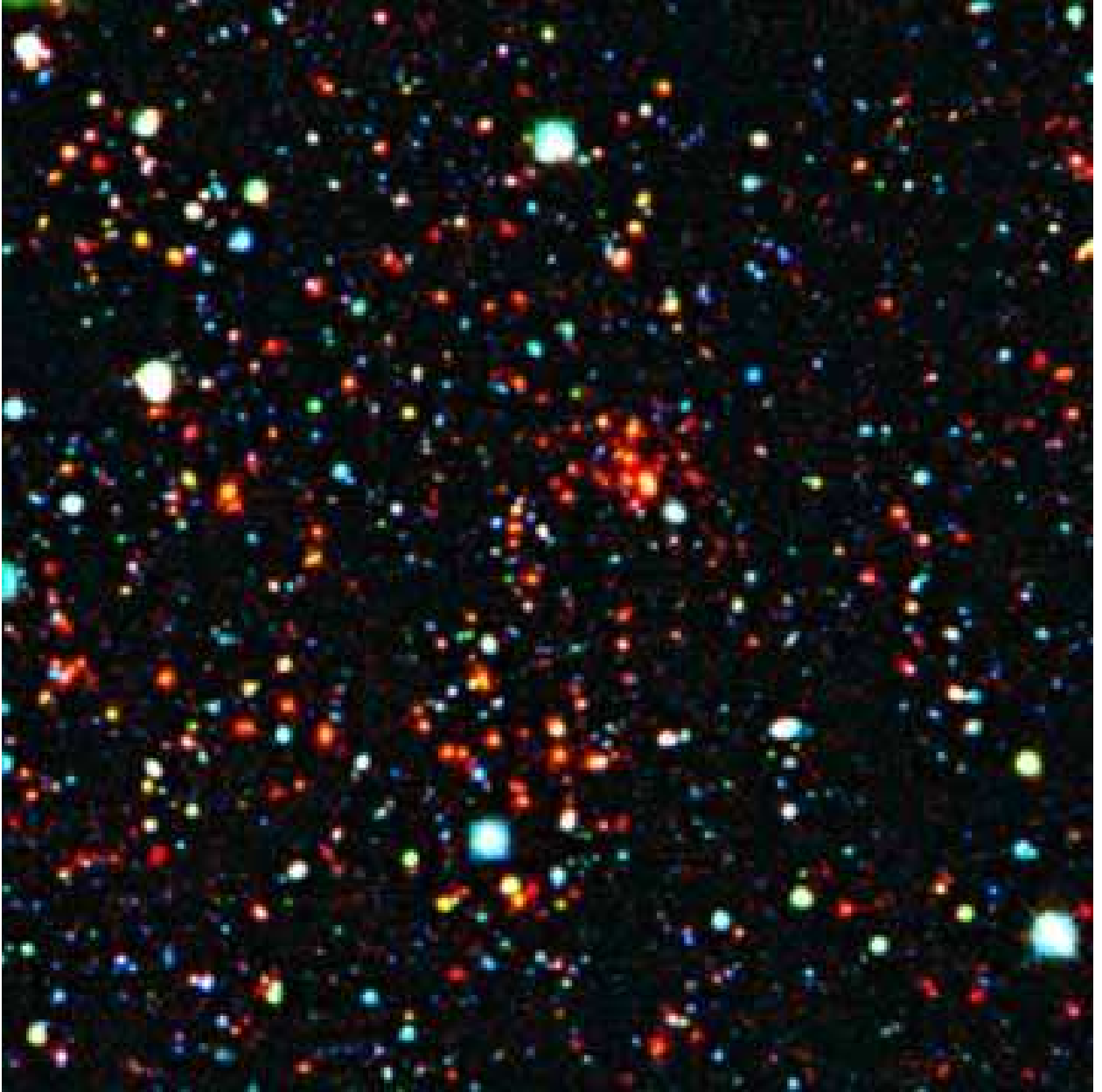


Fig. 6.— As for Figure 2, but for cluster ISCS J1432.4+3332 at  $\langle z_{\text{sp}} \rangle = 1.112$ .

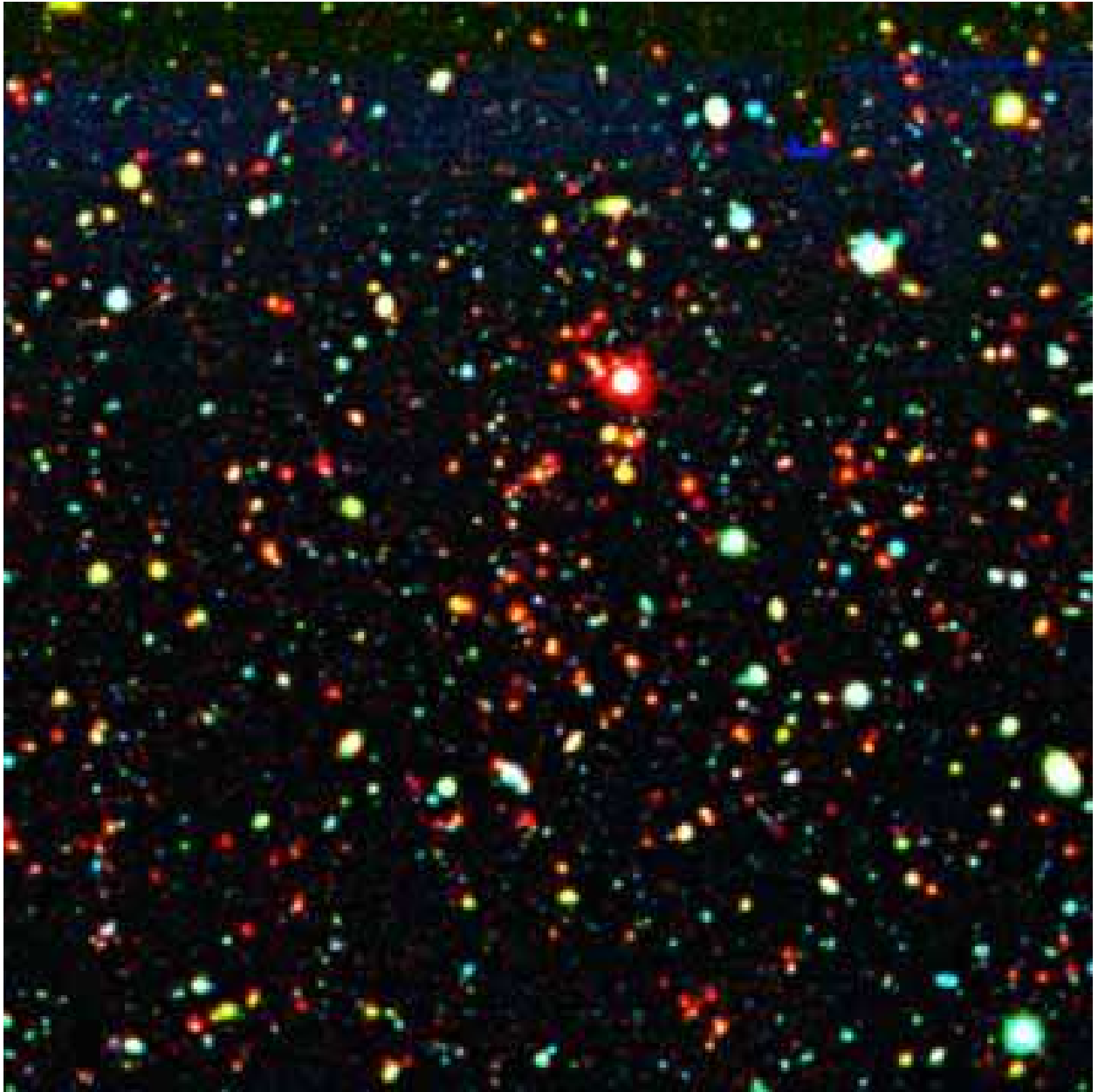


Fig. 7.— As for Figure 2, but for cluster ISCS J1426.1+3403 at  $\langle z_{\text{sp}} \rangle = 1.135$ .

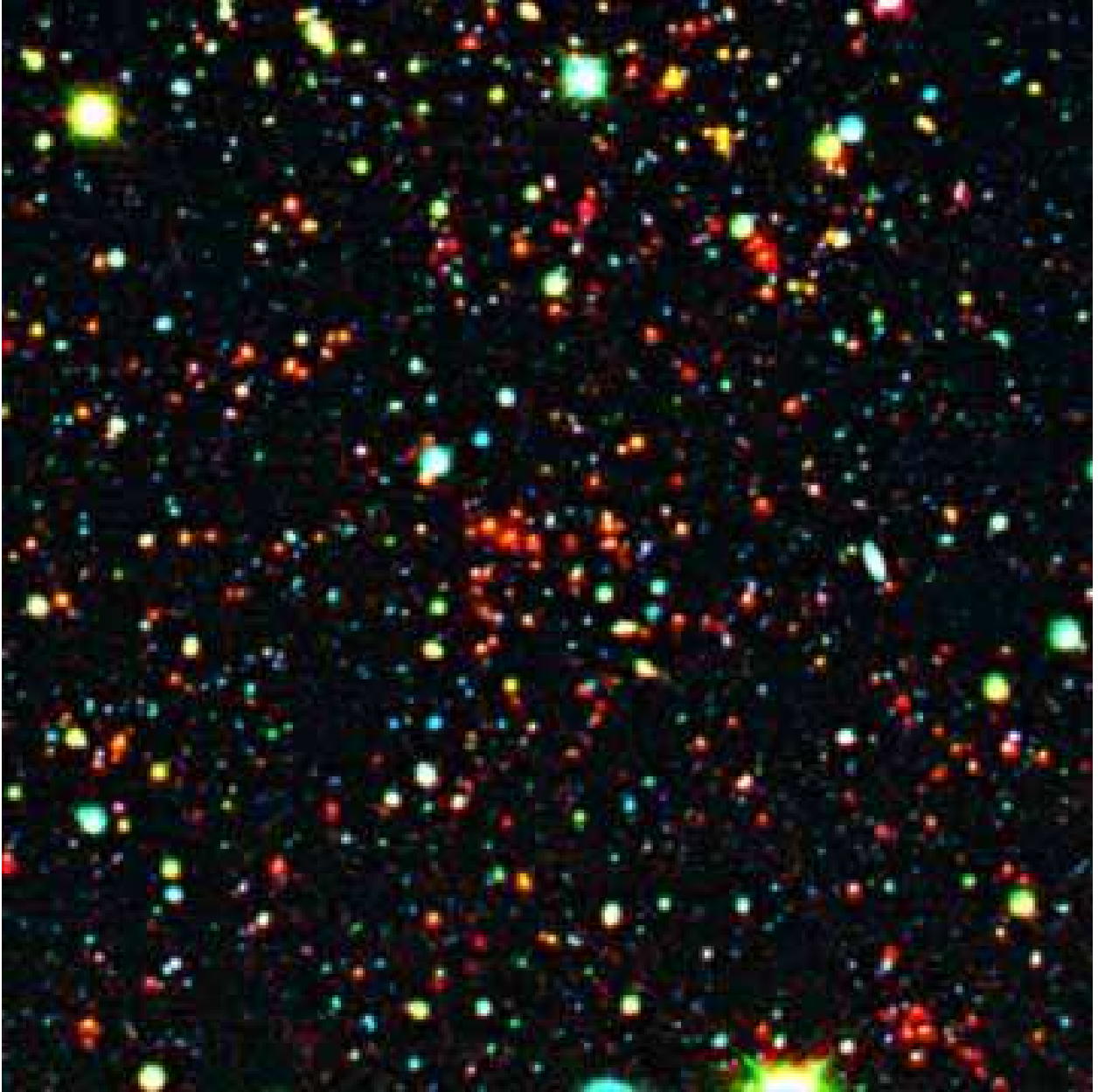


Fig. 8.— As for Figure 2, but for cluster ISCS J1426.5+3339 at  $\langle z_{\text{sp}} \rangle = 1.161$ .

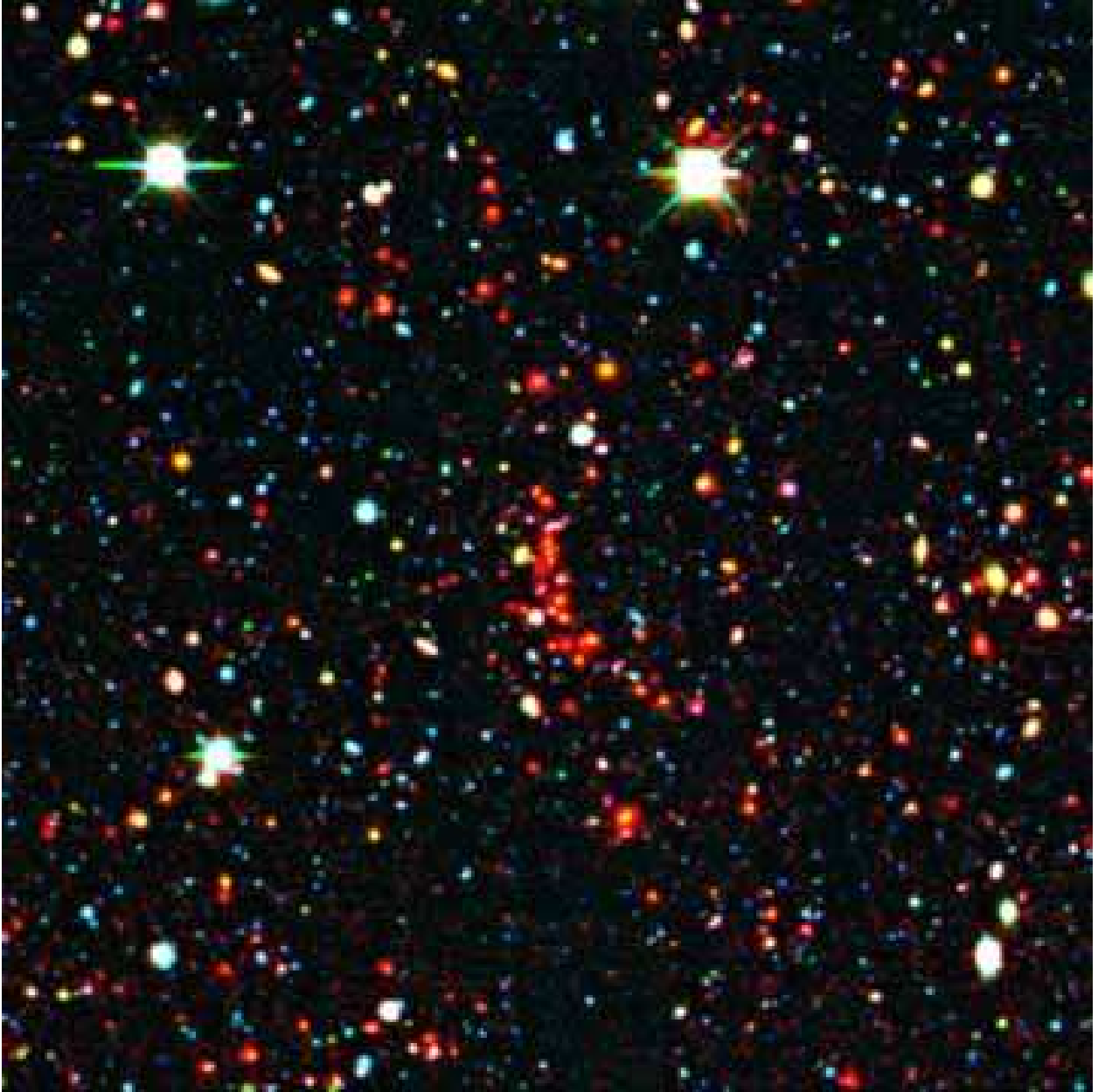


Fig. 9.— As for Figure 2, but for cluster ISCS J1434.5+3427 at  $\langle z_{\text{sp}} \rangle = 1.243$ .

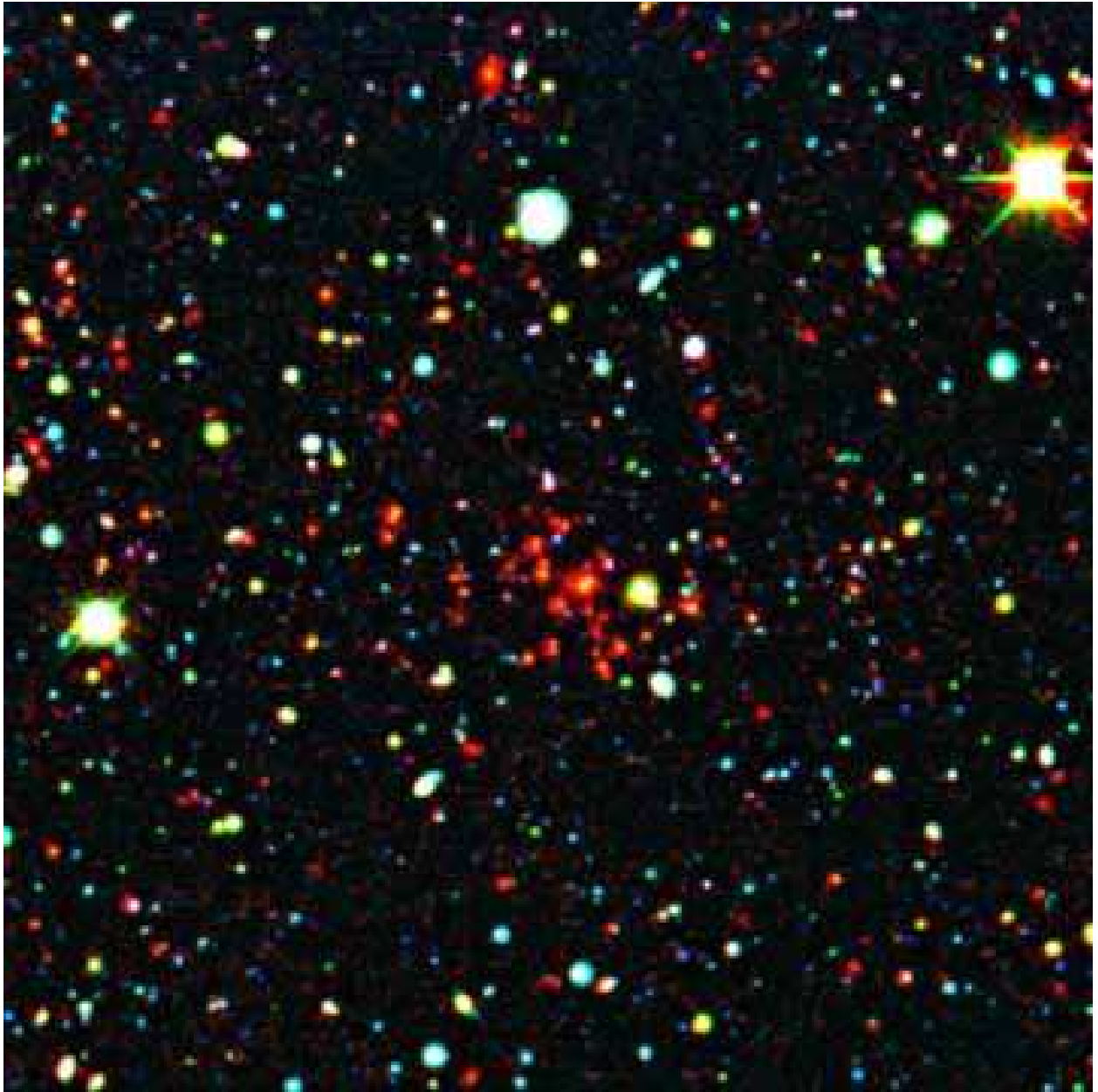


Fig. 10.— As for Figure 2, but for cluster ISCS J1429.3+3437 at  $\langle z_{\text{sp}} \rangle = 1.258$ .

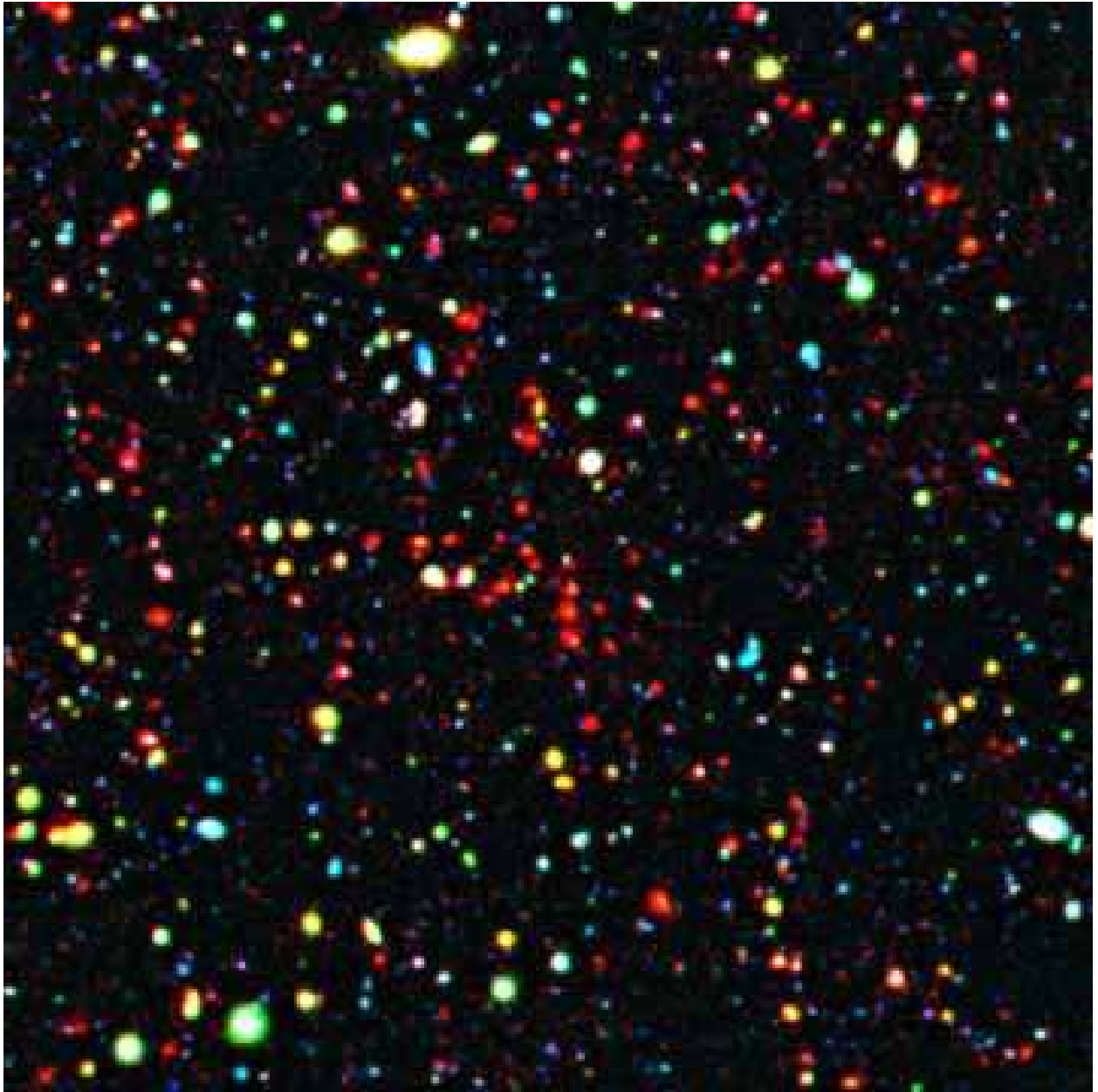


Fig. 11.— As for Figure 2, but for cluster ISCS J1432.6+3436 at  $\langle z_{\text{sp}} \rangle = 1.347$ .

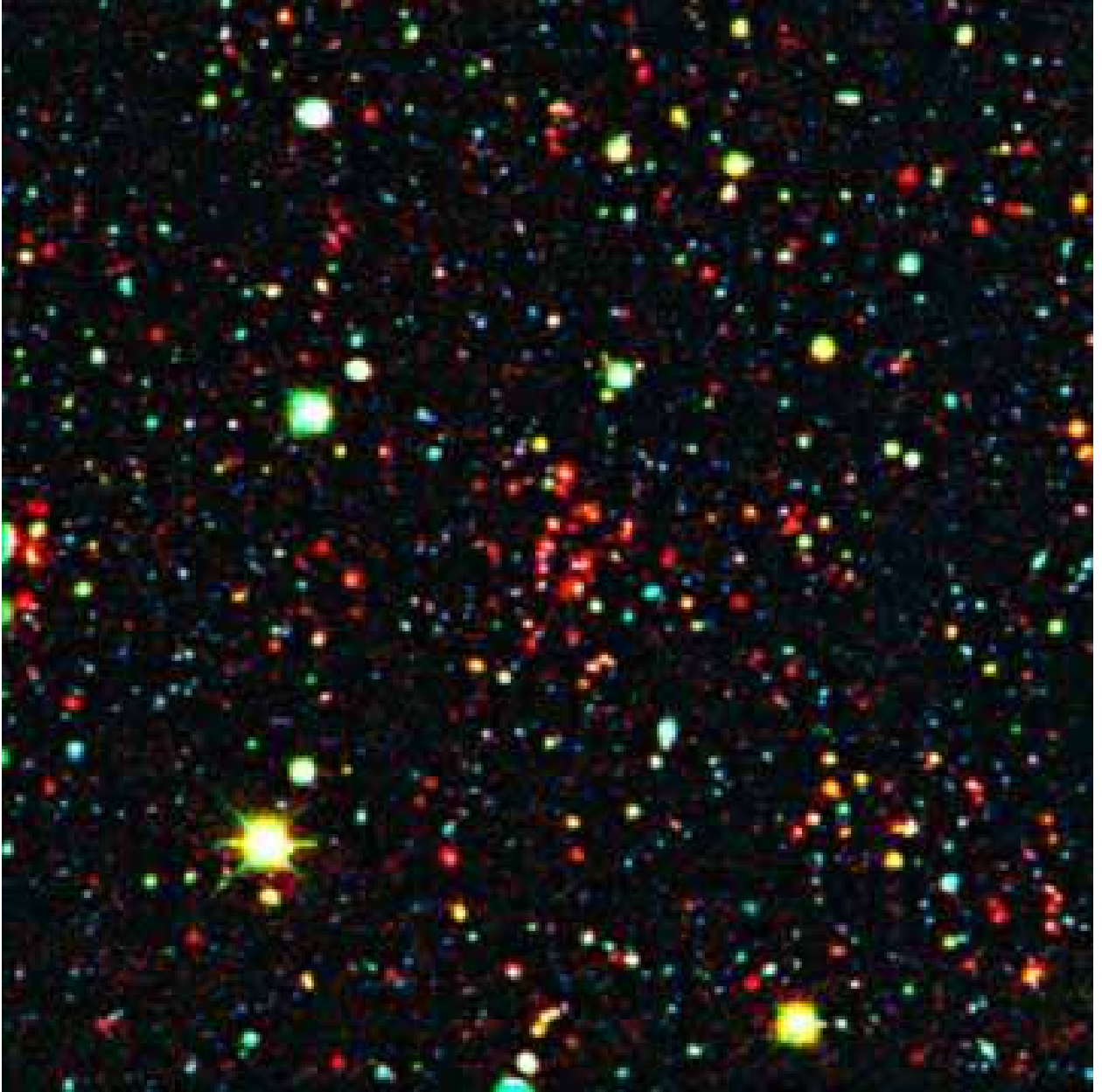


Fig. 12.— As for Figure 2, but for cluster ISCS J1434.7+3519 at  $\langle z_{\text{sp}} \rangle = 1.373$ .

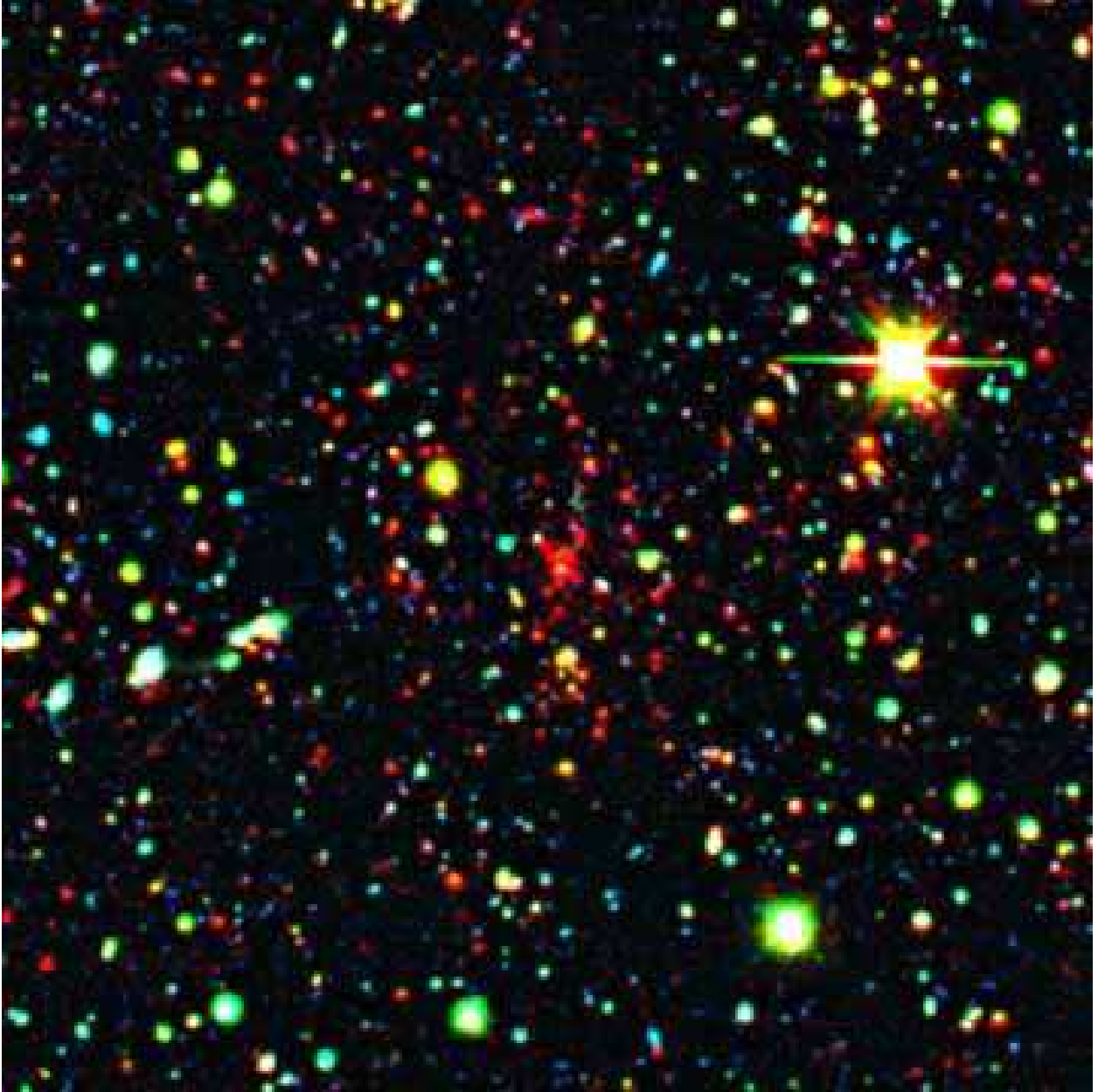


Fig. 13.— As for Figure 2, but for cluster ISCS J1438.1+3414 at  $\langle z_{\text{sp}} \rangle = 1.413$ .

unreported, spectroscopically confirmed cluster members, in declination order for IRAC sources, followed by serendipitous sources. Figure 14 shows three example spectra obtained in April 2007 with Keck/DEIMOS.

### 6.2.1. LRIS Observations

We obtained deep optical slitmask spectroscopy for several clusters using the dual-beam Low Resolution Imaging Spectrograph (LRIS; Oke et al. 1995) on the 10 m Keck I telescope during three observing runs between 2005 and 2007. Slitmasks generally included approximately 15 objects with photometric redshifts consistent with cluster membership and within 4 arcmin of the nominal cluster centers. Additional IRAC  $4.5\mu\text{m}$  selected sources were included to fill out the slitmasks. Slitlets had widths of 1.3 arcsec and minimum lengths of 10 arcsec. We employed the D580 dichroic which splits the light at  $\sim 5800 \text{ \AA}$  between the two channels of LRIS. On the red side, the 400 line grating, blazed at  $8500 \text{ \AA}$ , was used to cover a nominal wavelength range of  $5800$  to  $9800 \text{ \AA}$ , varying somewhat depending on the position of a slit in the mask. For objects filling a slitlet, the spectral resolution for this instrument configuration is  $\sim 9 \text{ \AA}$  ( $R \sim 900$ ), as determined from arc lamp spectra. On the blue side, the 400 line grism, blazed at  $3400 \text{ \AA}$ , provided coverage from the atmospheric cutoff ( $\sim 3200 \text{ \AA}$ ) up to the dichroic cut off. For objects filling a slitlet, the spectral resolution for this instrument configuration is  $\sim 8 \text{ \AA}$  ( $R \sim 450$ ).

We obtained multiple exposures for each mask, usually with 1800 s per individual exposure. Table 2 details the exposure times and observing conditions. The observations were carried out with the slitlets aligned close to the parallactic angle, and objects were shifted along the long axis of the slitlets between exposures to enable better sky subtraction and fringe correction.

The slitmask data were separated into individual spectra and then reduced using standard longslit techniques. The multiple exposures for each slitlet were reduced separately and then coadded. The spectra were reduced both without and with a fringe correction; the former tends to yield higher quality object spectra at the shorter wavelengths, while the latter is necessary at the longer wavelengths. Calibrations were obtained from arc lamp exposures taken immediately after the object exposures for the red side, and from arc lamp exposures taken during the afternoon for the blue side. Corrections for small offsets in the wavelength calibration were obtained by inspection of the positions of sky lines in the object spectra. Using longslit observations of the standard stars from Massey & Gronwall (1990) obtained during the same observing runs, we achieved relative flux calibration of the spectroscopy. While slit losses for resolved sources preclude absolute spectrophotometry from the slit mask

Table 2. Keck and Subaru Observations of  $z > 1$  ISCS Galaxy Clusters

Cluster	$\langle z_{\text{sp}} \rangle$	Inst.	UT Date	Exp. Time (s)	Conditions
ISCS_J1434.1+3328	1.057	DEIMOS	2007 Apr 18–19	$6 \times 1800$	clear; $0''.8 - 2''.0$
ISCS_J1429.2+3357	1.058	DEIMOS	2006 Apr 26	$4 \times 1500$	not photometric
ISCS_J1433.1+3334	1.070	DEIMOS	2007 Apr 19	$3 \times 1200$	clear; $0''.8$
ISCS_J1433.2+3324	1.096	DEIMOS	2007 Apr 18–19	$6 \times 1800$	clear; $0''.8 - 2''.0$
ISCS_J1432.4+3332	1.112	LRIS	2005 Jun 03	$5 \times 1800$	clear; $0''.9$ (Elston et al. 2006)
		FOCAS	2006 Apr 21	$5 \times 1200$	
		DEIMOS	2007 Apr 19	$3 \times 1200$	
ISCS_J1426.1+3403	1.135	LRIS	2007 May 19	$3 \times 1800$	clear; $0''.9$
ISCS_J1426.5+3339	1.161	LRIS	2006 Apr 04	$4 \times 1800$	clear
ISCS_J1434.5+3427	1.243	FOCAS	2006 Apr 22	$5 \times 1200$	likely cirrus; $1''.0 - 1''.5$
		DEIMOS	2007 Apr 18	$8 \times 1800$	
ISCS_J1429.3+3437	1.258	LRIS	2006 Apr 05	$3 \times 1200$	
ISCS_J1432.6+3436	1.347	LRIS	2007 May 21	$7 \times 1800$	mostly clear; $0''.8$
ISCS_J1434.7+3519	1.373	LRIS	2005 Jun 02	$7 \times 1800$	
ISCS_J1438.1+3414	1.413	FOCAS	2006 Jun 28	$9 \times 1200$	clear; $0''.9$
		DEIMOS	2007 Apr 19	$7 \times 1800$	

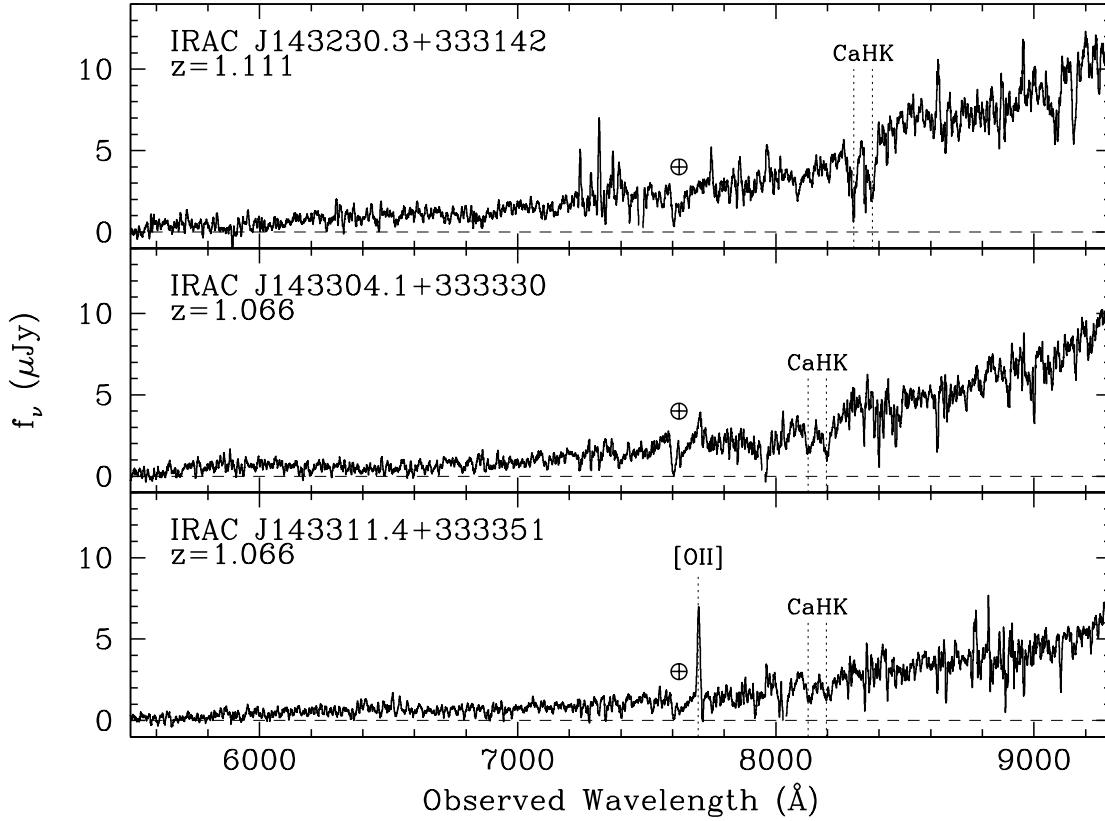


Fig. 14.— Optical spectra of three  $z > 1$  members of IRAC Shallow Survey clusters. The spectra were obtained with Keck/DEIMOS in April 2007 and flux calibrated using an archival sensitivity function. All three sources have class A spectra (§6) and show clear Ca H and K absorption, typical of early-type galaxies. The bottom source also shows strong [O II] emission, indicative of star formation. All three sources have  $I \sim 21.7$ . Imperfect sky subtraction is evident in the top spectrum near 7300 Å, and the 7600 Å atmospheric A-band is marked in all 3 panels.

data, the relative calibration of the spectral shapes should be accurate. One-dimensional spectra were extracted from the sum of all the reduced data for each slitlet for both the red and blue sides. For the targets in the high-redshift clusters, generally only the red side data proved useful.

### 6.2.2. DEIMOS Observations

Additional spectroscopy was obtained with the Deep Imaging Multi-Object Spectrograph (DEIMOS; Faber et al. 2003) on the 10 m Keck II telescope, a second generation instrument with significantly more multiplexing capabilities as compared to LRIS, albeit without the blue sensitivity. During an observing run in April 2006, we targeted Boötes active galaxy candidates selected on the basis of mid-infrared colors (e.g., Stern et al. 2005), but included candidate cluster members in one mask. In April 2007, while observing host galaxies of high redshift cluster supernovae (Perlmutter et al., in preparation), we also observed candidate cluster members, typically with more than one high redshift cluster candidate observed in each wide area mask.

For both observing runs, the 600ZD grating ( $\lambda_{\text{blaze}} = 7500 \text{ \AA}$ ;  $\Delta\lambda_{\text{FWHM}} = 3.7 \text{ \AA}$ ) and a GG455 order-blocking filter were used. DEIMOS data were processed using a slightly modified version of the pipeline developed by the DEEP2 team at UC-Berkeley<sup>4</sup>. Although neither run was completely photometric, relative flux calibration was achieved from observations of standard stars from Massey & Gronwall (1990).

## 6.3. Subaru Spectroscopy

Followup spectroscopic observations were also obtained with the FOCAS spectrograph (Kashikawa et al. 2002) on the 8.2-m Subaru telescope in April and June 2006. For these observations, we used the instrument in multi-object spectroscopy mode with 0.8 arcsec width slits, 300R grism, and SO58 order-sorting filter, which provided about 15 spectra from 5800Å to 10000Å with a spectral resolution  $R \sim 500$ . Total exposure times were 2-6 hours. The FOCAS data were reduced with IRAF using standard methods including a fringe correction. Wavelength calibration was done using OH airglow emission lines. Absolute flux was calibrated using standard star (Feige 34, Wolf 1346, Hz 44) spectra taken during the same nights.

---

<sup>4</sup>[http://astro.berkeley.edu/~sim\\$cooper/deep/spec2d/](http://astro.berkeley.edu/~sim$cooper/deep/spec2d/)

## 6.4. Notes on Individual Clusters

### 6.4.1. *ISCS J1434.1+3328* ( $z = 1.057$ )

ISCS J1434.1+3328 was observed with DEIMOS on a mask optimized for observing a high redshift supernova identified in a different ISCS high redshift cluster (Perlmutter et al., in preparation) which has not yet been spectroscopically confirmed. Four candidate members of ISCS J1434.1+3328 were targeted, and two more spectroscopic members were identified from additional slitlets targeting  $4.5 \mu\text{m}$  selected sources to fill the mask. All six confirmed members have clearly identified Ca H and K absorption lines and D4000 breaks, and none of the galaxies exhibit emission features in the wavelengths covered by the DEIMOS observations ( $\approx 5500 - 9500 \text{ \AA}$ ).

### 6.4.2. *ISCS J1429.2+3357* ( $z = 1.058$ )

ISCS J1429.2+3357 was observed with DEIMOS, on a slitmask optimized for observing faint, mid-infrared selected AGN candidates (e.g., Stern et al. 2005). Eight candidate cluster members were included in the slitmask, six of which were confirmed spectroscopically to reside at  $z \approx 1.06$ . Only the brightest galaxy, IRAC J142912.9+335808, shows [O II] emission; the remaining redshifts were derived on the basis of Ca H and K absorption lines and/or D4000 breaks. In addition, one galaxy targeted spectroscopically as an IRAC-selected AGN candidate, IRAC J142916.1+335537, is a cluster member, bringing the tally to seven spectroscopically confirmed cluster members. The spectrum of this source shows strong, narrow ( $400 \text{ km s}^{-1}$ ) emission lines from [Ne V]  $\lambda 3426$ , indicating that it is indeed an active galaxy.

### 6.4.3. *ISCS J1433.1+3334* ( $z = 1.070$ )

ISCS J1433.1+3334 was observed with DEIMOS on a mask optimized for observing a high redshift supernova identified in ISCS J1432.4+3332 (Perlmutter et al., in preparation). Eight candidate members of ISCS J1434.1+3328 were targeted, of which six were confirmed as cluster members, one was found to be slightly foreground to the cluster, and one was slightly behind the cluster. All eight candidates show clear D4000 breaks. Many additional cluster members were identified on this mask, either serendipitously or as targeted IRAC-selected,  $z > 1$  galaxies, bringing the total number of spectroscopically confirmed cluster members to 20. As seen in the bottom two panels of Figure 14, the confirmed sources show a range of spectral properties. While most show Ca H and K absorption and D4000 breaks,

some also show emission features likely due to either star formation or AGN activity.

*6.4.4. ISCS J1433.2+3324 ( $z = 1.096$ )*

ISCS J1433.2+3324 was observed with DEIMOS on the same mask as ISCS J1434.1+3328. Five candidate members of ISCS J1434.1+3328 were targeted, of which two were confirmed as cluster members, one was found to be foreground, and two yielded inconclusive spectra. Four additional cluster members were identified in the same mask, from IRAC-selected sources. The two confirmed cluster members which were specifically targeted show strong Ca H and K absorption and lack emission lines. The other four confirmed members all show [O II] emission, with three of the four also showing D4000 breaks.

*6.4.5. ISCS J1432.4+3332 ( $z = 1.112$ )*

The spectroscopic observations which confirmed ISCS J1432.4+3332 at  $z = 1.11$  are described in Elston et al. (2006), but no data on individual sources was presented there. The Elston et al. (2006) result was based on nine spectroscopically confirmed cluster members, two of which were selected not as cluster members, but rather as mid-IR selected AGN, and that data is now included in Table 3 of this paper. One of the candidate members of this cluster hosted a high-redshift supernova (Perlmutter et al., in preparation) and was thus targeted for additional DEIMOS and FOCAS slitmask spectroscopy. An example DEIMOS spectrum for this cluster is shown in the top panel of Figure 14. In total, there are now 23 spectroscopically confirmed members in the cluster.

*6.4.6. ISCS J1426.1+3403 ( $z = 1.135$ )*

Seven candidate members of this cluster were confirmed spectroscopically during our LRIS observations in May 2007. All seven galaxies show red continuum emission and/or a clear D4000 break. Two of the sources also show [O II] emission.

*6.4.7. ISCS J1426.5+3339 ( $z = 1.161$ )*

Four of the five spectroscopically confirmed members of this cluster show [O II] emission, a higher proportion than is typical for this program. This is possibly a selection effect; sources

with line emission are the easiest to spectroscopically confirm. All five confirmed members show breaks typical of early-type galaxies (e.g., D2900 and/or D4000).

*6.4.8. ISCS J1434.5+3427 ( $z = 1.243$ )*

This cluster is discussed in Brodwin et al. (2006), where eight spectroscopic members were presented. Table 3 of the current paper does not duplicate those data, and instead lists three additional spectroscopic members that have since been identified.

*6.4.9. ISCS J1429.3+3437 ( $z = 1.258$ )*

This cluster has nine spectroscopically confirmed members. One is an optically-bright AGN from the AGES survey, while the rest were confirmed spectroscopically by LRIS. Four of the Keck/LRIS sample show [O II] emission, while the other four show only spectral breaks and absorption lines.

*6.4.10. ISCS J1432.6+3436 ( $z = 1.347$ )*

This cluster has eight spectroscopically confirmed members, all from our Keck/LRIS observations in May 2007. Only one of the sources shows [O II] emission; the rest of the redshifts are on the basis of continuum breaks at 2640 and 2900 Å, as well as Mg II  $\lambda$  2800 absorption.

*6.4.11. ISCS J1434.7+3519 ( $z = 1.373$ )*

This cluster has five confirmed members, one of which was serendipitously identified in the spectroscopy, all from our Keck/LRIS spectroscopy in June 2005. Three of the members show [O II], and the other two show spectral breaks characteristic of early-type galaxy spectra.

6.4.12. *ISCS J1438.1+3414* ( $z = 1.413$ )

This cluster was first published in Stanford et al. (2005), at which time it was the highest redshift galaxy cluster known. Two candidate cluster members hosted supernovae in the *HST*/ACS program of Perlmutter et al. (in preparation), and this field thus has been the target of additional spectroscopy from Subaru and Keck. Five new cluster members have been confirmed, listed in Table 3. Data on the original five members is not duplicated from Stanford et al. (2005). Of the five new members, one is an [O II] emitter, serendipitously identified in a slitlet targeting another source. Three show only Ca H and K absorption lines, with no emission lines identified. IRAC J143816.8+341440 (22.3 in Table 3) is an AGN, showing [Ne IV], [O II], and [Ne III] emission lines.

## 6.5. Cluster Masses

With 20 or more spectroscopic redshifts, it is possible to estimate cluster masses via scaling relations using the velocity dispersion. The line of sight velocity dispersion for the 20 spectroscopic member galaxies in cluster 19 (ISCS J1433.1+3334) at  $z = 1.070$  is  $760 \text{ km s}^{-1}$  in the rest frame, and for the 23 spectroscopic member galaxies in cluster 17 (ISCS J1432.4+3332) at  $z = 1.112$  it is  $734 \text{ km s}^{-1}$ .

For these two clusters, which are among the richest in the sample, the velocity dispersion of  $\sim 750 \text{ km s}^{-1}$  corresponds to a virial mass of  $\sim 3.8 r_v \times 10^{14} M_\odot$  where  $r_v$  is the virial radius in Mpc (e.g. equation 4 of Carlberg et al. 1996). The x-ray temperature corresponding to  $\sigma = 750 \text{ km s}^{-1}$  is 3.9 keV (Table 4 of Xue & Wu 2000), which in turn gives a mass of  $\sim 4 \times 10^{14} M_\odot$  (Shimizu et al. 2003). This is consistent with the average halo mass of  $\sim 10^{14} M_\odot$  estimated by Brodwin et al. (2007) for the sample.

Stellar luminosities can also be used to make a rough estimate of cluster masses, scaling to the Coma cluster via the red spike model. Within the  $650 \times 850 \text{ kpc}$  region of Coma sampled by Eisenhardt et al. (2007) the integrated *K*-band luminosity to  $L^* + 1$  is  $54L^*$ , slightly higher than the values shown in column 11 of Table 1, but in a significantly smaller effective radius of 0.42 Mpc. In their Figure 1, Geller, Diaferio, & Kurtz (1999) show a mass for the Coma cluster of  $\sim 3.5 \times 10^{14} M_\odot$  within this radius (for  $h=0.7$ ). At  $r=1 \text{ Mpc}$  they show about double that mass, and suggest the total mass for Coma is about double this again. Hence if the profile and  $M/L_K$  for our clusters is similar to Coma, allowing for red spike model evolution in  $L_K$ , the  $L_{\text{tot}}/L^*$  values in 1 Mpc radius provided in Table 1 scale to total cluster masses of  $\sim 1 - 6 \times 10^{14} M_\odot$  (i.e.  $\sim 0.1 - 0.4 M_{\text{Coma}}$ ). Clusters 17 and 19 are at the top of this range, again providing mass estimates consistent with those found using

the velocity dispersion. More detailed exploration of this approach will require photometry which takes account of the extent to which a 5" diameter aperture fails to include all of the light from such galaxies, or includes light from multiple galaxies (as determined from higher spatial resolution imaging).

## 7. Discussion

As noted in the introduction, out to  $z \sim 1$  substantial evidence exists which is consistent with an extremely simple formation history for cluster galaxies, in which their stars are formed in a short burst at high redshift, and they evolve quiescently thereafter (ie a “red spike” model). The colors of luminous cluster galaxies out to  $z \sim 1$  typically fall on a tight sequence which is red relative to field galaxies at similar redshift (the “red sequence”), with a mean color which evolves as the red spike model predicts.

The most luminous red sequence galaxies are the reddest, a correlation which is attributed to higher metallicity in higher mass galaxies (Kodama & Arimoto 1997; but see also Ferreras & Silk 2003). This correlation (i.e the color-magnitude or mass-metallicity relation) is explained by additional cycles of star formation and enrichment in more massive galaxies, as they are able to retain their gas more effectively against supernovae-driven winds (Arimoto & Yoshii 1987). In the red spike formation paradigm, this is a natural consequence. In the context of the hierarchical merging galaxy formation models, a unique correlation between stellar mass and metallicity is a greater challenge. While the inclusion of feedback (whether by supernovae or by AGN) in hierarchical models stops the buildup of galaxy mass (e.g. Kauffmann & Charlot 1998; Nagashima & Yoshii 2004), such models have difficulty reproducing the exact color and slope of the color-magnitude relation in clusters over the full redshift range for which it has been measured. Recent work shows promise, however, as feedback behavior and other “gastrophysical” effects are taken more into account (e.g. De Lucia et al. 2006).

If the onset of the star formation “spike” is simultaneous for all cluster galaxies, and if the color-magnitude relation is caused by more protracted spikes in more massive galaxies, then as one approaches the star-forming epoch, massive galaxies might be expected to eventually become bluer, reversing the slope of the color-magnitude relation. In fact no measurable change is seen in color-magnitude slope out to  $z \sim 1$  (e.g Stanford et al. 1998; Mei et al. 2006), which suggests either formation redshifts well before  $z = 1$ , or that the spikes begin earlier in more massive galaxies, perhaps ending rather than beginning simultaneously. The small and unchanging scatter of the red sequence in clusters out to  $z \sim 1$  (e.g. Stanford et al. 1998; Blakeslee et al. 2003; Tran et al. 2007) also argues for synchronized or very early spikes

and against a primarily age-based origin of the color-magnitude relation, since the scatter would increase by a much larger amount, and faster, than has been observed.

Testing to what extent red spike models remain consistent with cluster galaxy data at  $z > 1$  is one of the primary motivations for the present study. We begin by constructing the color-magnitude relations for the 12 spectroscopically confirmed clusters in Table 1.

### 7.1. Color-Magnitude Diagrams

Figures 15 and 16 present color magnitude diagrams for the clusters listed in Table 1. The  $I - [3.6]$  color was selected because these filters bracket the 4000Å break most tightly at  $z > 1$ . The symbol area is proportional to the integral of the object’s redshift probability distribution over the range  $z_{\text{est}} \pm 0.06(1 + z_{\text{est}})$ , which is the rms dispersion in individual photometric redshifts (Brodwin et al. 2006). Circled symbols are spectroscopically confirmed members, while crosses indicate objects known *not* to be members on the basis of spectroscopy. Figures 15 and 16 include objects within 1 Mpc of the cluster center, with  $> 5\sigma$  detections in both  $[3.6]$  and  $[4.5]$ , and with  $> 2\sigma$  detections in  $I$ ; or with spectroscopic redshifts. As noted in §3.2, the  $5\sigma$  limit in  $[3.6]$  is 18.6 mag, so the limiting factor in object selection for Figures 15 and 16 is from the  $5\sigma$  limit of 17.8 mag in  $[4.5]$ . We have used the 0.1 Gyr burst,  $z_f = 3$  red spike model shown in Figure 1 to calculate the corresponding  $[3.6]$  mag as a function of redshift, and this is shown in Figures 15 and 16 by the vertical dotted lines. The  $I$  limit is shown by the diagonal dotted lines in Figures 15 and 16. The vertical dashed line plots the expected  $L^*$  magnitude at  $[3.6]$  for the red spike model. The sloped dashed line shows the observed  $U - H$  color-magnitude slope of 0.22 for the Coma cluster from the data of Eisenhardt et al. (2007), normalized at the red spike model  $[3.6]$  magnitude and  $I - [3.6]$  color for an  $L^*$  galaxy. In this redshift range observed  $I - [3.6]$  is close to rest  $U - H$ . Note that while the normalization evolves according to the red spike model, a constant, *unevolving* slope value is used.

The brightest galaxy likely to be a member is typically 1 to 2 magnitudes brighter than the expected  $L^*$  magnitude for the red spike model (see Table 1). It is noteworthy that the brightest galaxy in the Coma cluster is  $\approx 6$  times brighter than  $L^*$  in the  $H$  band (de Propris et al. 1998; Eisenhardt et al. 2007), suggesting less than a factor of two growth in stellar mass in such galaxies since  $z \sim 1.5$ . *HST* imaging should be used to assess this more carefully.

Because these clusters were *not* selected on the basis of containing a red sequence (§5), the fact that the highest probability cluster members tend to track the passively evolving

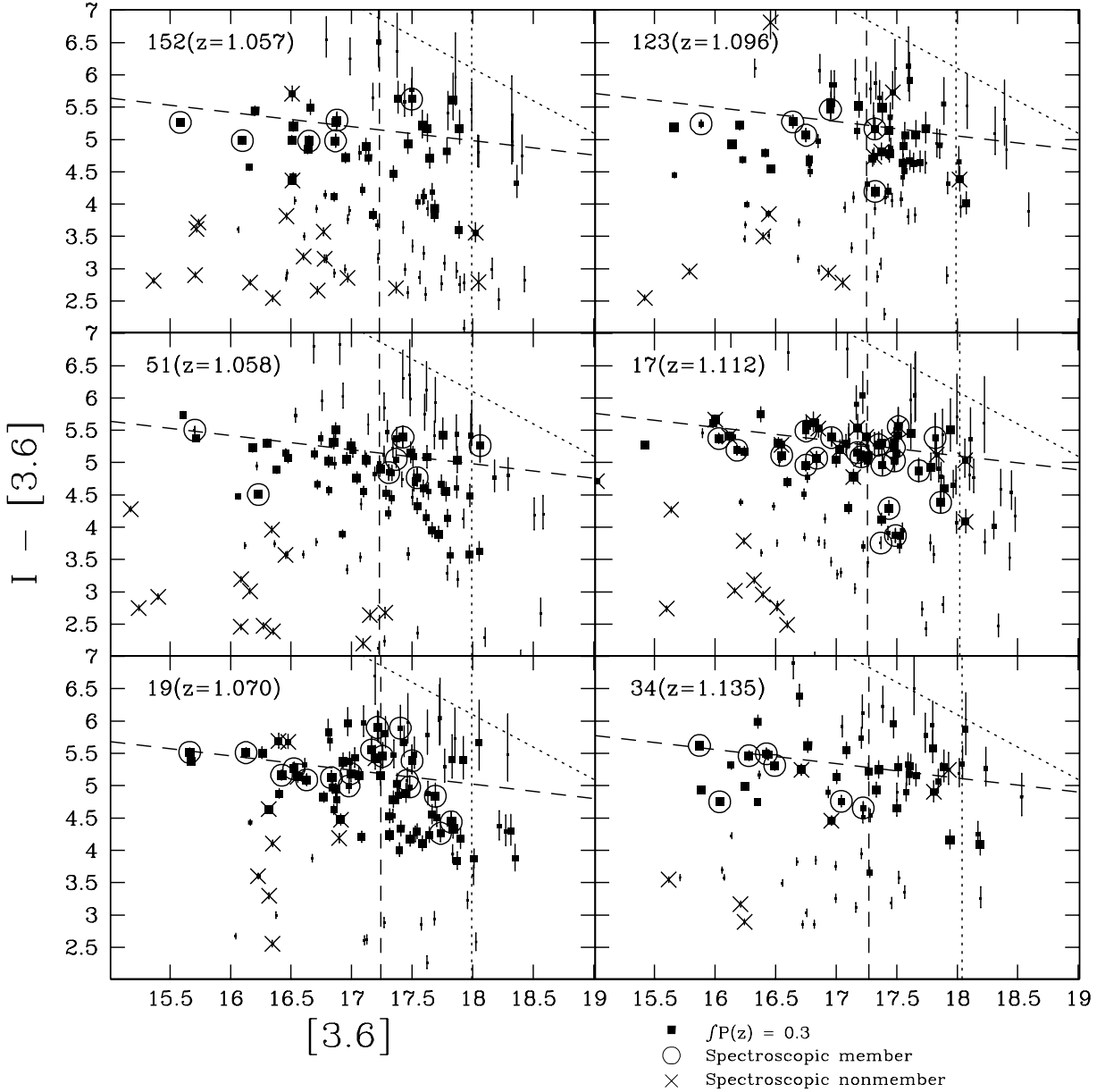


Fig. 15.— Observed  $I - [3.6]$  vs.  $[3.6]$  for galaxies within 1 Mpc of the center of the spectroscopically confirmed clusters at  $z > 1$ , in order of increasing redshift. The catalog number and spectroscopic redshift for each cluster from Table 1 are given in the upper left corner of each sub-panel. The symbol area is proportional to the galaxy’s integrated redshift probability in the range  $z_{\text{est}} \pm 0.06(1 + z_{\text{est}})$ . A symbol with an integrated probability of 0.3 is shown for reference in the lower right portion of the figure. Additional details are provided in §7.1.

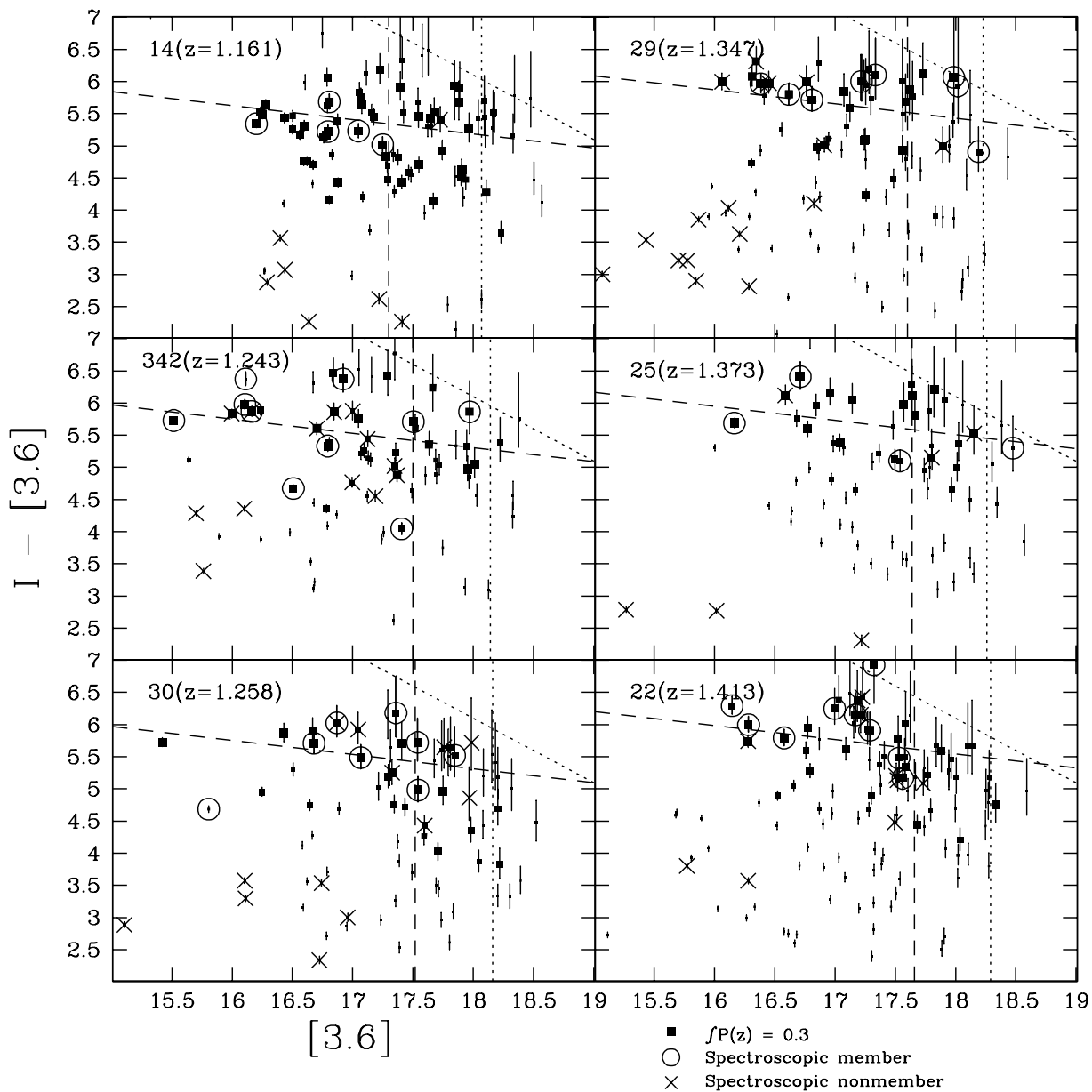


Fig. 16.— Observed  $I - [3.6]$  vs.  $[3.6]$  for the remainder of the spectroscopically confirmed clusters at  $z > 1$ , in order of increasing redshift. See figure 15 for details.

Coma cluster sequence shown by the dashed line is significant. Evidently the red sequence persists in dense environments to  $z = 1.4$ , even when not used as a selection criterion. In addition there is no indication that the slope of the color-magnitude relation has changed sign, and in fact a non-evolving Coma cluster slope appears consistent with the data.

Comparing the data for e.g. cluster 14 (ISCS J1426.5+3339 at  $z = 1.16$ ) vs. 29 (ISCS J1432.6+3436 at  $z = 1.34$ ) suggests real differences in the scatter of the color-magnitude relation do exist. The presence of luminous galaxies substantially bluer than the red sequence in several clusters, a number of them spectroscopically confirmed, is also noteworthy. These may represent a population of massive star-forming galaxies which fade onto the red sequence in rich clusters, but is not found in field surveys (e.g. Bell et al. 2004). It should be noted that the very low scatters reported for  $z > 1$  clusters in e.g. Blakeslee et al. (2003) and Mei et al. (2006) are calculated for galaxies known to have early-type morphologies, using much deeper photometry than the survey/discovery data used here. Further investigation of the color-magnitude relations is deferred to a future paper which will use deeper *Spitzer* and *HST* imaging presently being obtained.

Although the survey data used to identify the clusters does not enable accurate photometry of individual galaxies in clusters, we can calculate mean properties for galaxies in each cluster with some confidence. In the next section we briefly explore the color evolution and color-magnitude relation of the entire cluster sample.

## 7.2. Color vs. Redshift

Figure 17 plots the average  $I - [3.6]$  color for galaxies within 1 Mpc of the cluster centers, and whose integrated redshift probability distribution in the range  $z_{\text{est}} \pm 0.06(1 + z_{\text{est}})$  exceeds 0.3. The mean values are calculated after iteratively clipping  $3\sigma$  outliers. As implied by the color-magnitude diagrams for the spectroscopically confirmed clusters (§7.1), the red spike model (0.1 Gyr burst at  $z_f = 3$ ) provides a remarkably good fit to the empirical data, validating the survey design assumptions illustrated in Figure 1.

Much of the increase in  $I - [3.6]$  with redshift is due to the change in the rest frame wavelengths observed, and in Figure 18 we plot the average color relative to a no-evolution model (i.e. the k-corrected color). The no-evolution model is simply the red spike model at  $z=0$ , i.e. at an age of 11.3 Gyr for the stellar population. Clearly the evolving red spike model is a better fit to the data than is the k-correction alone. Note that the photometric redshifts (§4) are calculated using *non*-evolving templates, so this result is not a foregone conclusion, particularly at  $z > 1$ .

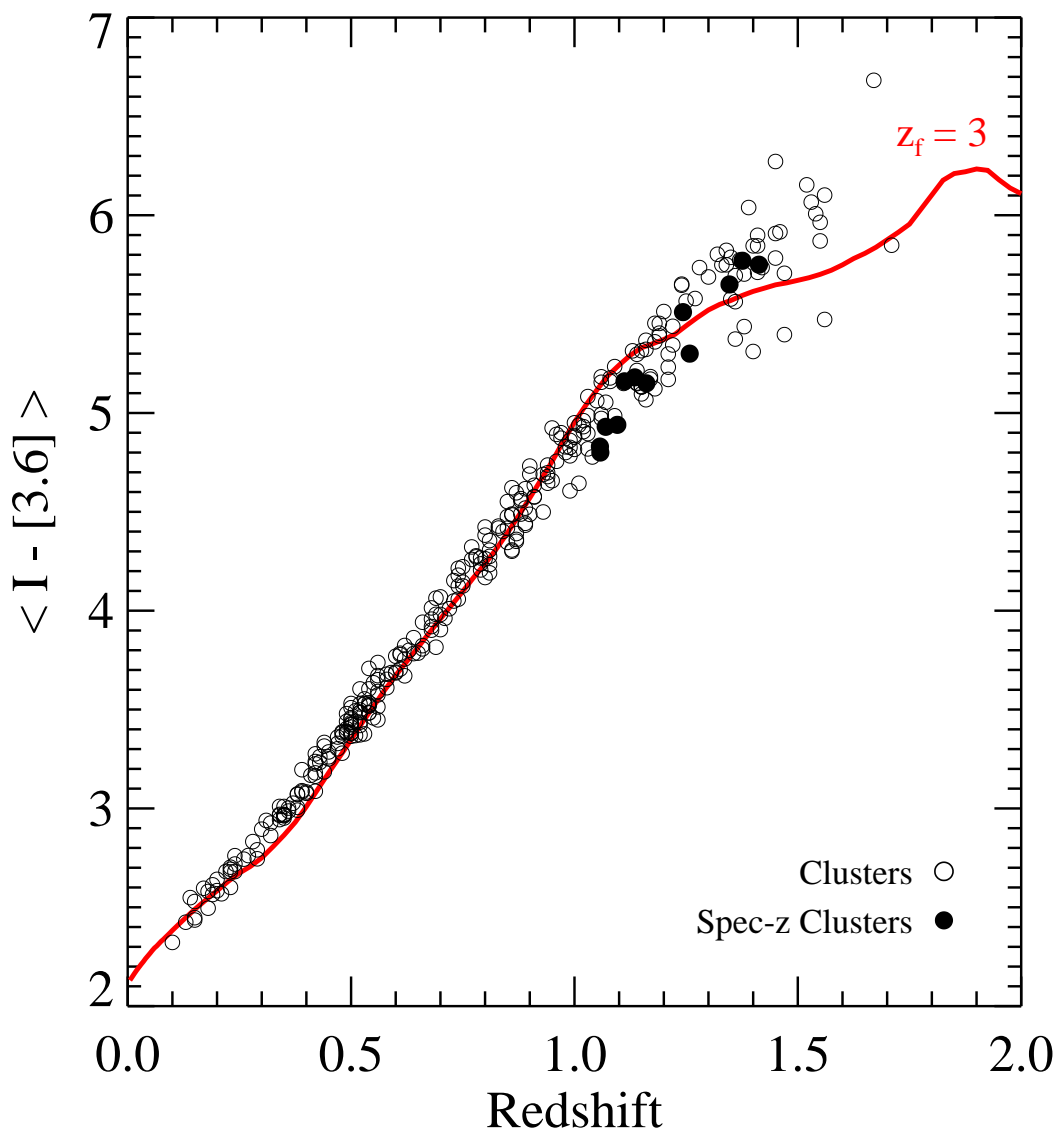


Fig. 17.— Mean observed  $I - [3.6]$  vs estimated cluster redshift  $z_{\text{est}}$  for galaxies within 1 Mpc of the cluster center and with integrated redshift probabilities  $> 0.3$  in the range  $z_{\text{est}} \pm 0.06(1 + z_{\text{est}})$ . The solid red line is the predicted  $I - [3.6]$  color for the red spike model. Filled symbols show the mean  $I - [3.6]$  colors for the spectroscopically confirmed  $z > 1$  clusters listed in Table 1.

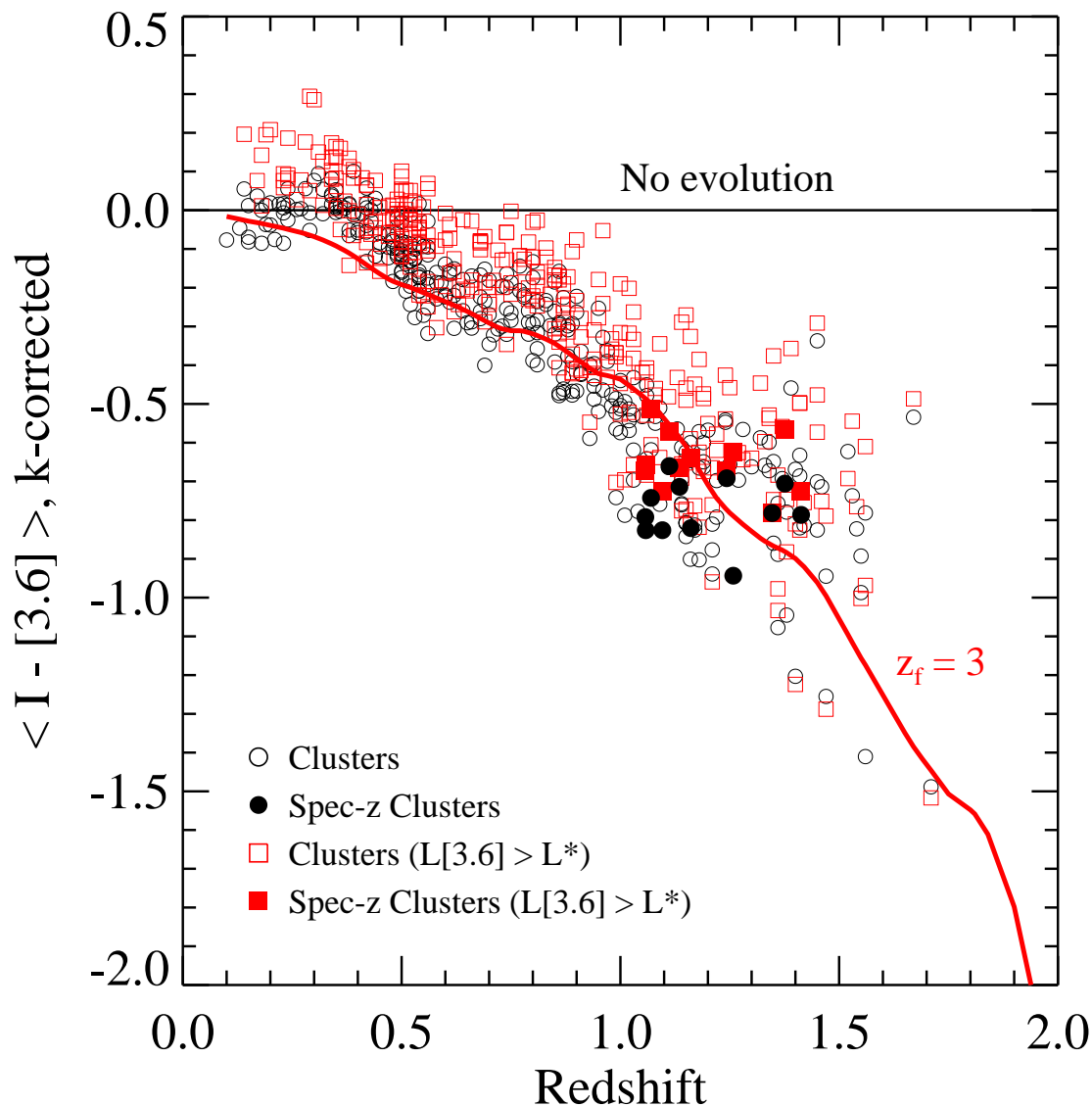


Fig. 18.— As for Figure 17, but with the k-correction subtracted. Red squares are the mean observed  $I - [3.6]$  for galaxies brighter than the expected  $[3.6]$  magnitude for an  $L^*$  galaxy for the red spike model. The solid red line is the predicted  $I - [3.6]$  color for the red spike model. Filled symbols show the mean  $I - [3.6]$  colors for the spectroscopically confirmed  $z > 1$  clusters listed in Table 1.

The mean  $I - [3.6]$  colors in Figure 17 include galaxies down to the  $13.3\mu\text{Jy}$  survey limit at  $4.5\mu\text{m}$ , and therefore less luminous galaxies contribute to the mean at lower redshifts. The color-magnitude relation shows that less luminous galaxies are bluer, and massive galaxies are quite quiescent today, so a constant flux limit will lead to a systematic bias towards more luminous, massive galaxies and redder mean color with increasing redshift. On the other hand the excellent fit of the red spike model implies that a constant *luminosity* limit for the sample would select galaxies with smaller stellar masses at high redshift, since a constant stellar mass, passively evolving, will be more luminous as one approaches the formation redshift. To avoid this bias, in Figure 18 we also show (with red squares) the mean colors for galaxies brighter than the red spike passively-evolving  $L^*$  in [3.6].

It is evident that the mean color of the more luminous galaxies is systematically redder, and hence that the color-magnitude relation continues to hold out to  $z \sim 1.5$ . The color offset is 0.1 magnitudes, independent of redshift. The persistence of the essentially unchanged color-magnitude relation slope, with a passively evolving intercept, out to lookback times within 4 Gyr of the Big Bang is a phenomenon that models of cluster galaxy formation must account for. The implication is that the correlation between high stellar population metallicity and stellar mass is already in place at  $z \sim 1.5$ , and that the star formation era remains well in the past for these galaxies.

In Figure 19 the mean  $I - [3.6]$  colors are plotted with the predicted  $I - [3.6]$  color for the red spike model subtracted. The mean colors are for galaxies more luminous in [3.6] than the red spike  $L^*$ . Note the red spike model is a good match to  $L^*$  galaxy colors in figures 17 and 18, so the offset in color out to  $z \sim 1$  is attributable to the color-magnitude relation.

Other effects may be in play. In Table 1 the  $z_{\text{est}}$  values tend to be lower than the  $\langle z_{\text{sp}} \rangle$  values, which may lead to colors appearing  $\sim 0.1$  mag redder relative to the red spike model than if  $\langle z_{\text{sp}} \rangle$  were available for all  $z > 1$  clusters. The average colors of cluster members may still be redder than shown, however, as no attempt has been made to correct the average cluster colors for field contamination, and field galaxies tend to be bluer than cluster galaxies. Blending issues could lead to colors which are systematically biased. Given these uncertainties, the excellent agreement with the red spike model is the more remarkable. Nevertheless, at  $z > 1$  the trend is towards colors which are increasingly redder than the red spike model, for both the full sample and the spectroscopically confirmed subset, though there is clearly a range. Hence even higher formation redshifts (as high as  $z_f = 30$ ) are favored for most  $z > 1$  clusters, within the context of red spike models.

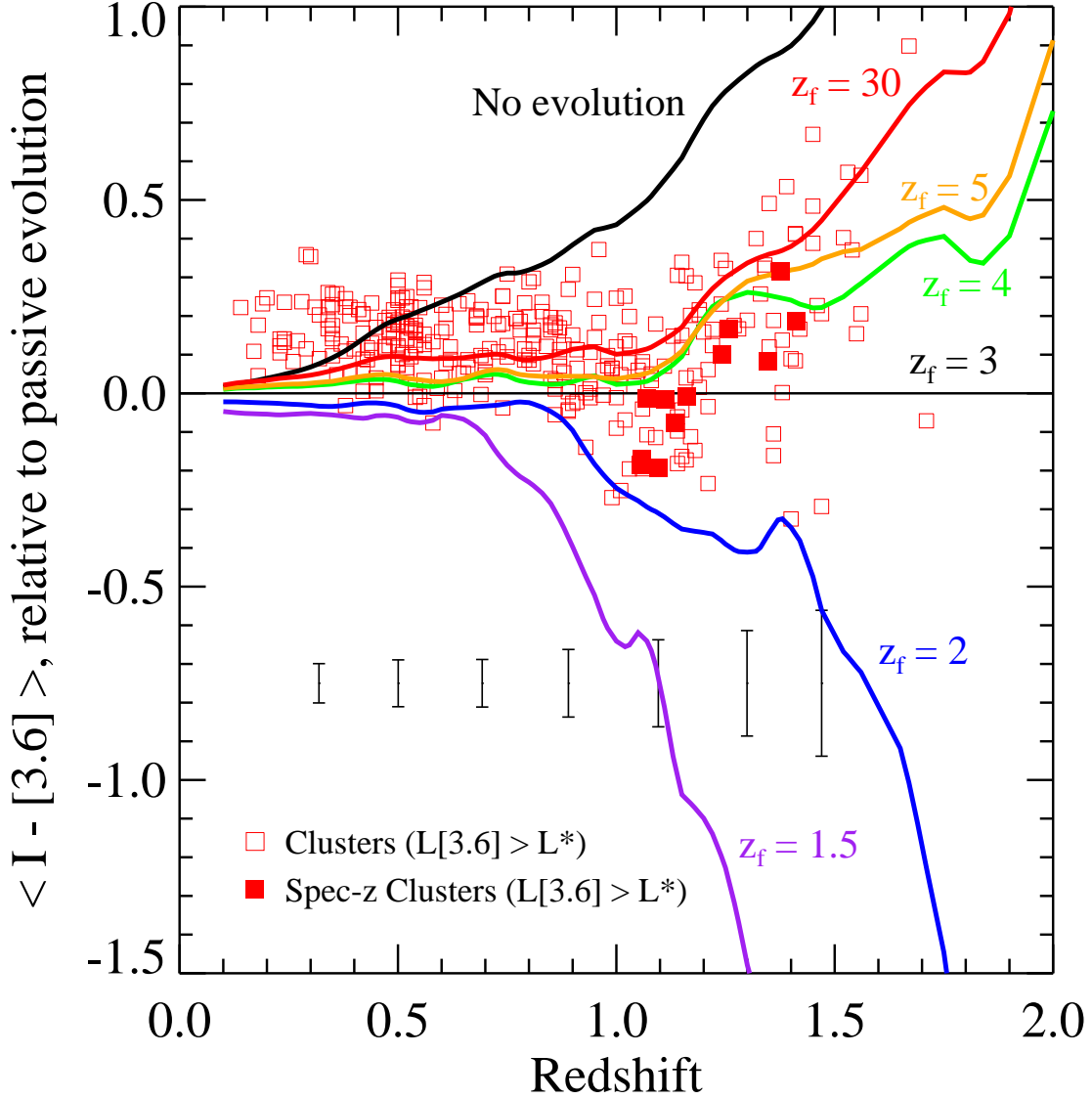


Fig. 19.— As for Figure 17, but with predicted  $I - [3.6]$  color for the red spike model subtracted. Means are shown only for galaxies brighter than the expected  $[3.6]$  magnitude for an  $L^*$  galaxy for the red spike model. The black horizontal line is the 0.1 Gyr burst,  $z_f = 3$  (red spike) model prediction. The purple, blue, green, orange, red, and black lines show the expected relative  $I - [3.6]$  color for a 0.1 Gyr burst starting at  $z_f = 1.5, 2, 4, 5, 30$ , and for no evolution (k-correction) respectively. Representative values of the uncertainty in each cluster's mean  $I - [3.6]$  color are shown at several redshifts. Filled symbols show the mean  $I - [3.6]$  colors for the spectroscopically confirmed  $z > 1$  clusters listed in Table 1.

### 7.3. Clusters at $1.5 < z < 2$

Figure 17 shows that there are relatively few cluster candidates in the IRAC sample with  $z_{\text{est}} > 1.5$ . Why is this? The red spike model fits, circumstantial evidence from BCG luminosity, and the persistence of the color-magnitude relation suggest that the stellar populations were formed – and assembled – well before  $z \sim 1.5$ . From Figure 1, such clusters should be detectable by the IRAC Shallow Survey.

A potential selection effect against  $z > 1.5$  galaxies is that photometric redshifts in this range have increasingly broad redshift probability distributions, due in part to insufficient depth in photometry at shorter wavelengths. Simulations indicate a factor of two reduction in IRAC photometric error can help compensate, leading to a similar reduction in photometric redshift error in this redshift range. With the *Spitzer* Deep Wide-Field Survey legacy program now underway (PI D. Stern), such data will be available in the near future. The tighter redshift probability distributions would improve the contrast of high redshift clusters over the field, allowing them to meet our detection threshold.

But the lack of massive  $z > 1.5$  cluster detections may simply reflect a real decline in the space density of such objects. Models for the hierarchical growth of structure predict only about 1 cluster with  $z > 1.4$  above  $10^{14}M_{\odot}$  for every 5 clusters with  $z > 1$ . Full exploration of this possibility will require more careful simulation and assessment of our observational selection effects.

## 8. Summary

We have identified 335 galaxy cluster and group candidates from a  $4.5\mu\text{m}$  selected sample of galaxies in the IRAC Shallow Survey. Candidates were identified by searching for overdensities in photometric redshift slices, and 106 clusters are at  $z > 1$ . Roughly 10% of these candidates may be expected to arise by chance or from projection effects. To date, 12 clusters have been spectroscopically confirmed at  $z > 1$ , as have 61 of the 73 clusters observed with AGES at  $z < 0.5$ . For the two  $z > 1$  clusters with 20 or more spectroscopic members, total cluster masses of several  $10^{14}M_{\odot}$  are indicated, and the total mass estimated from the stellar luminosity yields comparable values. Color-magnitude diagrams in  $I - [3.6]$  vs.  $[3.6]$  for the  $z > 1$  spectroscopically confirmed clusters reveal that a red sequence is generally present, even though clusters were not selected for this. The brightest probable member galaxy (at the spatial resolution of IRAC) in the spectroscopically confirmed  $z > 1$  clusters remains 1 – 2 mag brighter than the passively-evolving  $L^*$  luminosity. For the full cluster sample, the mean color of brighter galaxies within each cluster is systematically redder than

the mean color of all probable cluster member galaxies, implying that the mass-metallicity relation is already in place at  $z \sim 1.5$ . The mean  $I - [3.6]$  color of probable cluster members is well fit by a simple model in which stars form in a 0.1 Gyr burst beginning at  $z_f = 3$ . At  $z > 1$  there is a tendency for mean cluster colors to favor formation redshifts  $z_f > 3$ , although a few are consistent with  $z_f \sim 2$ . This adds to the large body of evidence that galaxies in clusters were established at extremely early times.

We thank Mark Dickinson, Emily MacDonald, and Hyron Spinrad for generously making time available on their scheduled nights for the DEIMOS observations reported here. Naoki Yasuda, Naohiro Takanashi, Yutaka Ihara, Kohki Konishi, and Hiroyuki Utsunomiya assisted with observations at the Subaru Telescope. Roberto De Propris provided the integrated luminosity for Coma cluster galaxies. Thoughtful comments from the anonymous referee improved the presentation of this work. The IRAC Shallow Survey was executed using guaranteed observing time contributed by G. Fazio, G. and M. Rieke, M. Werner, and E. Wright. This work is based in part on observations made with the *Spitzer Space Telescope*, which is operated by the Jet Propulsion Laboratory, California Institute of Technology under a contract with NASA. This work made use of images and data products provided by the NOAO Deep Wide-Field Survey, which is supported by the National Optical Astronomy Observatory (NOAO). NOAO is operated by AURA, Inc., under a cooperative agreement with the National Science Foundation. Some of the data presented herein were obtained at the W.M. Keck Observatory, which is operated as a scientific partnership among the California Institute of Technology, the University of California and the National Aeronautics and Space Administration. The Observatory was made possible by the generous financial support of the W.M. Keck Foundation. Some of the data presented were collected at the Subaru Telescope, which is operated by the National Astronomical Observatory of Japan. The work of SAS was performed under the auspices of the U.S. Department of Energy, National Nuclear Security Administration, by the University of California, Lawrence Livermore National Laboratory, under contract No. W-7405-Eng-48. The work of KD and JM was partially supported by the Director, Office of Science, Department of Energy, under grant DE-AC02-05CH11231.

## REFERENCES

- Abell, G. O. 1958, *ApJS*, 3, 211
- Andreon, S., Valtchanov, I., Jones, L. R., Altieri, B., Bremer, M., Willis, J., Pierre, M., & Quintana, H. 2005, *MNRAS*, 359, 1250
- Arendt, R. G. et al. 1998, *ApJ*, 508, 74

- Arimoto, N. & Yoshii, Y. 1987, *A&A*, 173, 23
- Bahcall, N. A. & Bode, P. 2003, *ApJ*, 588, L1
- Bell, E. F. et al. 2004, *ApJ*, 608, 752
- Bertin, E. & Arnouts, S. 1996, *A&AS*, 117, 393
- Blakeslee, J. P. et al. 2003, *ApJ*, 596, L143
- Brodwin, M. et al. 2006, *ApJ*, 651, 791
- Brodwin, M., Gonzalez, A. H., Moustakas, L. A., Eisenhardt, P. R., Stanford, S. A., Stern, D. & Brown, M. J. I. 2007, *ApJ*, 671, L93
- Brown, M. J. I., Jannuzi, B. T., Dey, A., & Tiede, G. P. 2005, *ApJ*, 621, 41
- Bruzual, G. & Charlot, S. 2003, *MNRAS*, 344, 1000
- Carlberg, R. G., Yee, H. K. C., Ellingson, E., Abraham, R., Gravel, P., Morris, S., & Pritchet, C. J. 1996, *ApJ*, 462, 32
- Coleman, G. D., Wu, C.-C., & Weedman, D. W. 1980, *ApJS*, 43, 393
- Cool, R. J. 2007, *ApJS*, 169, 21
- De Lucia, G., Springel, V., White, S. D. M., Croton, D., & Kauffmann, G. 2006, *MNRAS*, 366, 499
- de Propris, R., Eisenhardt, P. R., Stanford, S. A., & Dickinson, M. 1998, *ApJ*, 503, L45
- de Propris, R., Stanford, S. A., Eisenhardt, P. R., Dickinson, M., & Elston, R. 1999, *AJ*, 118, 719
- De Propris, R., Stanford, S. A., Eisenhardt, P. R., Holden, B. P., & Rosati, P. 2007, *AJ*, 133, 2209
- de Vries, W. H., Morganti, R., Röttgering, H. J. A., Vermeulen, R., van Breugel, W., Rengelink, R., & Jarvis, M. J. 2002, *AJ*, 123, 1784
- Eisenhardt, P. R., De Propris, R., Gonzalez, A. H., Stanford, S. A., Wang, M., & Dickinson, M. 2007, *ApJS*, 169, 225
- Eisenhardt, P. R. et al. 2004, *ApJS*, 154, 48

- Elston, R. J., Gonzalez, A. H., et al. 2006, *ApJ*, 639, 816
- Faber, S. M. et al. 2003, in *Instrument Design and Performance for Optical/Infrared Ground-based Telescopes*. Proceedings of the SPIE, Volume 4841, ed. M. Iye & A. F. M. Moorwood, 1657–1669
- Fazio, G. G. et al. 2004a, *ApJS*, 154, 39
- . 2004b, *ApJS*, 154, 10
- Ferreras, I. & Silk, J. 2003, *MNRAS*, 344, 455
- Geller, M. J., Diaferio, A., & Kurtz, M. J. 1999, *ApJ*, 517, L23
- Gladders, M. D. & Yee, H. K. C. 2000, *AJ*, 120, 2148
- . 2005, *ApJS*, 157, 1
- Gladders, M. D., Yee, H. K. C., Majumdar, S., Barrientos, L. F., Hoekstra, H., Hall, P. B., & Infante, L. 2007, *ApJ*, 655, 128
- Hetterscheidt, M., Simon, P., Schirmer, M., Hildebrandt, H., Schrabback, T., Erben, T., & Schneider, P. 2007, *A&A*, 468, 859
- Hoekstra, H., Mellier, Y., van Waerbeke, L., Semboloni, E., Fu, L., Hudson, M. J., Parker, L. C., Tereno, I., & Benabed, K. 2006, *ApJ*, 647, 116
- Hoekstra, H., Yee, H. K. C., & Gladders, M. D. 2002, *ApJ*, 577, 595
- Houck, J. R. et al. 2005, *ApJ*, 622, L105
- Jannuzi, B. T. & Dey, A. 1999, in *ASP Conf. Ser. 191: Photometric Redshifts and the Detection of High Redshift Galaxies*, ed. R. Weymann, L. Storrie-Lombardi, M. Sawicki, & R. Brunner, 111
- Kashikawa, N. et al. 2002, *PASJ*, 54, 819
- Kauffmann, G. & Charlot, S. 1998, *MNRAS*, 294, 705
- Kenter, A. et al. 2005, *ApJS*, 161, 9
- Kinney, A. L., Calzetti, D., Bohlin, R. C., McQuade, K., Storchi-Bergmann, T., & Schmitt, H. R. 1996, *ApJ*, 467, 38

- Kneissl, R., Jones, M. E., Saunders, R., Eke, V. R., Lasenby, A. N., Grainge, K., & Cotter, G. 2001, *MNRAS*, 328, 783
- Kodama, T. & Arimoto, N. 1997, *A&A*, 320, 41
- Kosowsky, A. 2003, *New Astronomy Review*, 47, 939
- Loh, M. et al. 2005, *American Astronomical Society Meeting Abstracts*, 207, 41.01
- Massey, P. & Gronwall, C. 1990, *ApJ*, 358, 344
- McCarthy, P. J. et al. 2007, *ApJ*, 664, L17
- Mei, S. et al. 2006, *ApJ*, 644, 759
- Miller, C. J. et al. 2005, *AJ*, 130, 968
- Mullis, C. R., Rosati, P., Lamer, G., Böhringer, H., Schwobe, A., Schuecker, P., & Fassbender, R. 2005, *ApJ*, 623, L85
- Murray, S. S. et al. 2005, *ApJS*, 161, 1
- Nagashima, M. & Yoshii, Y. 2004, *ApJ*, 610, 23
- Oke, J. B. et al. 1995, *PASP*, 107, 375
- Olsen, L. F. et al. 1999, *A&A*, 345, 681
- Ouchi, M. & SXDS. 2007, *American Astronomical Society Meeting Abstracts*, 210, 97.02
- Overzier, R. A. et al. 2006, *ApJ*, 637, 58
- Pentericci, L. et al. 2000, *A&A*, 361, L25
- Postman, M., Lubin, L. M., Gunn, J. E., Oke, J. B., Hoessel, J. G., Schneider, D. P., & Christensen, J. A. 1996, *AJ*, 111, 615
- Reach, W. T. et al. 2005, *PASP*, 117, 978
- Rosati, P., Borgani, S., & Norman, C. 2002, *ARA&A*, 40, 539
- Rosati, P., Stanford, S. A., Eisenhardt, P. R., Elston, R., Spinrad, H., Stern, D., & Dey, A. 1999, *AJ*, 118, 76
- Rosati, P. et al. 2004, *AJ*, 127, 230

- Ruhl, J. et al. 2004, in *Astronomical Structures and Mechanisms Technology. Proceedings of the SPIE*, Volume 5498, ed. J. Zmuidzinas, W. S. Holland, & S. Withington, 11–29
- Scoddeggio, M. et al. 1999, *A&AS*, 137, 83
- Sheth, R. K. & Tormen, G. 1999, *MNRAS*, 308, 119
- Shimizu, M., Kitayama, T., Sasaki, S., & Suto, Y. 2003, *ApJ*, 590, 197
- Spergel, D. N. et al. 2003, *ApJS*, 148, 175
- . 2007, *ApJS*, 170, 377
- Stanford, S. A., Eisenhardt, P. R., & Dickinson, M. 1998, *ApJ*, 492, 461
- Stanford, S. A., Elston, R., Eisenhardt, P. R., Spinrad, H., Stern, D., & Dey, A. 1997, *AJ*, 114, 2232
- Stanford, S. A., Holden, B., Rosati, P., Eisenhardt, P. R., Stern, D., Squires, G., & Spinrad, H. 2002, *AJ*, 123, 619
- Stanford, S. A. et al. 2005, *ApJ*, 634, L129
- . 2006, *ApJ*, 646, L13
- Steidel, C. C., Adelberger, K. L., Dickinson, M., Giavalisco, M., Pettini, M., & Kellogg, M. 1998, *ApJ*, 492, 428
- Steidel, C. C., Adelberger, K. L., Shapley, A. E., Erb, D. K., Reddy, N. A., & Pettini, M. 2005, *ApJ*, 626, 44
- Stern, D. et al. 2005, *ApJ*, 631, 163
- Strazzullo, V. et al. 2006, *A&A*, 450, 909
- Toft, S., Mainieri, V., Rosati, P., Lidman, C., Demarco, R., Nonino, M., & Stanford, S. A. 2004, *A&A*, 422, 29
- Tran, K.-V. H., Franx, M., Illingworth, G. D., van Dokkum, P., Kelson, D. D., Blakeslee, J. P., & Postman, M. 2007, *ApJ*, 661, 750
- Valtchanov, I. et al. 2004, *A&A*, 423, 75
- van Breukelen, C. et al. 2006, *MNRAS*, L107

Venemans, B. P. et al. 2002, ApJ, 569, L11

—. 2005, A&A, 431, 793

Vikhlinin, A., McNamara, B. R., Forman, W., Jones, C., Quintana, H., & Hornstrup, A.  
1998, ApJ, 502, 558

Werner, M. W. et al. 2004, ApJS, 154, 1

Wilson, G. et al. 2006, astro-ph/0604289

Xue, Y.-J., & Wu, X.-P. 2000, ApJ, 538, 65

Yamada, T. et al. 2005, ApJ, 634, 861

Zatloukal, M., Röser, H.-J., Wolf, C., Hippelein, H., & Falter, S. 2007, A&A, 474, L5

Table 3.  $z > 1$  Spectroscopic Cluster Members

ID <sup>a</sup>	[4.5] <sup>b</sup>	phot- $z$	spec- $z$
ISCS_J1434.1+3328 $\langle z_{\text{sp}} \rangle = 1.057$			
152.1	15.45	1.01	1.057
152.2	15.99	0.91	1.055
152.3	17.00	0.96	1.054
152.4	17.47	1.04	1.065
152.5	16.40	0.99	1.055
152.6	16.76	0.96	1.055
ISCS_J1429.2+3357 $\langle z_{\text{sp}} \rangle = 1.058$			
51.1	15.10	0.98	1.059
51.2	17.06	0.95	1.056
51.3	17.83	1.04	1.055
51.4	17.16	1.00	1.060
51.5	17.01	1.03	1.059
51.6	17.19	1.03	1.054
51.7	16.08	1.01	1.060
ISCS_J1433.1+3334 $\langle z_{\text{sp}} \rangle = 1.070$			
19.1	17.49	0.99	1.075
19.2	16.67	0.99	1.075
19.3	17.04	1.06	1.076
19.4	16.00	1.06	1.066
19.5	16.89	1.09	1.067
19.6	16.47	0.94	1.065
19.7	17.70	1.00	1.063
19.8	17.15	1.10	1.079
19.9	16.75	0.98	1.074
19.10	16.30	1.07	1.066
19.11	16.21	1.03	1.066
19.12	16.66	1.03	1.075
19.13	15.44	1.06	1.064
19.14	17.03	1.28	1.076
19.15	17.51	1.00	1.065

Table 3—Continued

ID <sup>a</sup>	[4.5] <sup>b</sup>	phot- <i>z</i>	spec- <i>z</i>
19.16	17.01	1.27	1.069
19.17	17.36	1.04	1.066
19.18	16.27	0.86	1.063
19.19	16.68	2.45	1.074
19.20 <sup>c</sup>	-	-	1.067
ISCS_J1433.2+3324 $\langle z_{\text{sp}} \rangle = 1.096$			
123.1	15.32	1.07	1.094
123.2	16.45	1.09	1.093
123.3	16.68	1.10	1.094
123.4	16.99	1.11	1.107
123.5	16.64	0.93	1.094
123.6	17.35	0.99	1.091
ISCS_J1432.4+3332 $\langle z_{\text{sp}} \rangle = 1.112$			
17.1	16.94	2.74	1.1120
17.2	17.35	1.03	1.1108
17.3	16.48	1.07	1.111
17.4	15.97	1.05	1.115
17.5	16.31	1.04	1.111
17.6	15.85	1.09	1.110
17.7	16.04	1.35	1.121
17.8	17.57	1.20	1.116
17.9	16.87	1.00	1.11
17.10	17.31	1.04	1.1086
17.11	17.01	1.14	1.098
17.12	17.43	1.12	1.105
17.13	17.51	0.98	1.109
17.14	17.32	0.91	1.112
17.15	16.59	1.07	1.104
17.16	16.92	1.19	1.119
17.17	17.42	1.09	1.115
17.18	17.33	1.11	1.115

Table 3—Continued

ID <sup>a</sup>	[4.5] <sup>b</sup>	phot- <i>z</i>	spec- <i>z</i>
17.19	17.29	1.06	1.118
17.20	16.90	1.18	1.107
17.21	16.38	1.26	1.115
17.22 <sup>c</sup>	-	-	1.114
17.23 <sup>c</sup>	-	-	1.110
ISCS_J1426.1+3403 $\langle z_{\text{sp}} \rangle = 1.135$			
34.1	16.35	1.03	1.1439
34.2	15.75	1.04	1.1301
34.3	16.01	1.11	1.1271
34.4	15.69	1.00	1.1328
34.5	16.12	1.18	1.134
34.6	16.90	0.91	1.13
34.7	17.24	0.89	1.144
ISCS_J1426.5+3339 $\langle z_{\text{sp}} \rangle = 1.161$			
14.1	16.87	1.10	1.16
14.2	15.96	1.05	1.157
14.3	16.44	1.19	1.1631
14.4	16.64	1.17	1.1634
14.5	16.88	1.04	1.1637
ISCS_J1434.5+3427 $\langle z_{\text{sp}} \rangle = 1.243$ <sup>d</sup>			
342.1	16.76	1.21	1.240
342.2	17.71	1.21	1.251
342.3 <sup>c</sup>	-	-	1.256
ISCS_J1429.3+3437 $\langle z_{\text{sp}} \rangle = 1.258$			
30.1	16.65	1.18	1.245
30.2	16.39	1.13	1.26
30.3	17.24	1.15	1.2576
30.4	17.37	1.07	1.263
30.5	17.41	1.29	1.2611
30.6	16.86	1.08	1.2583
30.7	16.97	1.31	1.2582

Table 3—Continued

ID <sup>a</sup>	[4.5] <sup>b</sup>	phot- <i>z</i>	spec- <i>z</i>
30.8	15.19	0.97	1.2632
30.9 <sup>c</sup>	-	-	1.2546
ISCS_J1432.6+3436 $\langle z_{\text{sp}} \rangle = 1.347$			
29.1	17.63	1.26	1.3559
29.2	17.61	1.25	1.35
29.3	16.39	1.32	1.35
29.4	16.06	1.21	1.3320
29.5	17.55	1.40	1.347
29.6	16.77	1.29	1.347
29.7	16.86	1.30	1.34
29.8	16.14	1.26	1.353
ISCS_J1434.7+3519 $\langle z_{\text{sp}} \rangle = 1.373$			
25.1	17.52	3.33	1.37
25.2	16.98	1.53	1.372
25.3	16.28	1.34	1.37
25.4	15.68	1.33	1.374
25.5 <sup>c</sup>	-	-	1.380
ISCS_J1438.1+3414 $\langle z_{\text{sp}} \rangle = 1.413$ <sup>e</sup>			
22.1	15.86	1.25	1.411
22.2	15.79	1.38	1.418
22.3	16.91	1.38	1.412
22.4	16.76	1.35	1.414
22.5 <sup>c</sup>	-	-	1.412

<sup>a</sup>Coordinates will appear in published version.

<sup>b</sup>Vega magnitude at  $4.5\mu\text{m}$ ; 0 mag = 179.5 Jy.

<sup>c</sup>Serendipitous                      spectroscopic

source not included in  $5\sigma$   $4.5\mu\text{m}$  catalog.

<sup>d</sup>Additional spectroscopic members for ISCS J1434.5+3427 published in Brodwin et al. (2006)

<sup>e</sup>Additional spectroscopic members for ISCS J1438.1+3414 published in Stanford et al. (2005)